2010

4-D Modeling of Displacement Vector Fields for Improved Radiation Therapy

Elizabeth Zachariah
Virginia Commonwealth University

4-D Modeling of Displacement Vector Fields for Improved Radiation Therapy

A thesis submitted in partial fulfillment of the requirements for the degree of Master of Science at Virginia Commonwealth University.

by

Elizabeth Shobha Zachariah
Bachelor of Science
Virginia Commonwealth University
May 2008

Director: Ding-Yu Fei, Ph.D.
Associate Professor
Department of Biomedical Engineering

Virginia Commonwealth University
Richmond, Virginia
December, 2010

ACKNOWLEDGEMENT

First of all I would like to thank Dr. Docef for being a great and patient advisor and for helping me throughout this experience. I want to also acknowledge my advisors, Dr. Fei and Dr. Bai, for the guidance and expertise they shared with me. One person I want to especially thank is my mentor Dr. Filippas. She has done so much for me the past four years. I know that without her, I would not be able to be where I am today. She has been a great role model for me, and I want her to know that I really appreciate her.

Finally, I want to thank my family for all the support and strength they have given me. Nothing in this world would be possible for me without the help of my father, mother, and sister. They have encouraged me to work hard for my dreams, and I want them to know that I am very proud to have them as my family.

TABLE OF CONTENTS

LIST OF TABLES

LIST OF FIGURES

Abstract

4-D MODELING OF DISPLACEMENT VECTOR FIELDS FOR IMPROVED RADIATION THERAPY

By Elizabeth Shobha Zachariah
Bachelor of Science, Virginia Commonwealth University, May 2008

A thesis submitted in partial fulfillment of the requirements for the degree of Master of Science at Virginia Commonwealth University.

Virginia Commonwealth University, 2010.

Major Director: Ding-Yu Fei, Ph.D. Associate Professor, Department of Biomedical Engineering

In radiation therapy, it is imperative to deliver high doses of radiation to the tumor while reducing radiation to the healthy tissue. Respiratory motion is the most significant source of errors during treatment. Therefore, it is essential to accurately model respiratory motion for precise and effective radiation delivery. Many approaches exist to account for respiratory motion, such as controlled breath hold and respiratory gating, and they have been relatively successful. They still present many drawbacks. Thus, research has been expanded to tumor tracking. This paper presents a spatio-temporal model for four dimensional CT reconstruction. The method begins with a set of initial CT projections and a simultaneously acquired breathing trace. Two methods are explored to model the spatial components: principal component analysis and a pseudoinverse matrix method. An iterative approach is used to match the simulated projections to the actual projections. The

simulated projections and the initial projections are evaluated using Normalized Root Mean Square Error (NRMSE). The proposed method shows simulated projections and actual projections match, and as such the model is able to accurately predict the deformation.

CHAPTER 1
INTRODUCTION

Radiation therapy procedures, by tradition, have used imaging technology for initial treatment planning. The technology has predominantly been used to generate scans of the patient's anatomy to identify the tumor size and location preceding the treatment [1,2]. Currently, imaging technology such as computed tomography (CT) has been used before, during, and after radiation therapy for treatment planning, guidance, and verification [3-5].

Because radiation therapy requires the acquisition of multiple CT scans, it is important to consider reducing the ionizing radiation a patient receives. Properly radiating a tumor inhibits the tumor's ability to reproduce; however, normal tissue is also radiated along with the tumor [6]. The normal tissue is then damaged, because it also loses its ability to reproduce. Therefore, it is important to accurately predict the location and geometry of the tumor [1]. Image-guided radiation therapy (IGRT) is a prominent method used to increase accuracy in dose-targeting. IGRT uses numerous and repetitive imaging to improve the localization of the target tissue by tracking the changes of the target during the radiation delivery [4,7].

A critical tool in the acquisition of data for IGRT is time-dependent computed tomography (ordinarily denoted as 4DCT). 4DCT is able to image the movement of the anatomy [8]. It is principally used to account for respiratory motion. As such, 4DCT

requires a large amount of data to reconstruct a time sequence of CTs from scratch [2]. Numerous methods have been implemented to construct a 4DCT model of the moving anatomy. Some methods include modeling respiratory motion with cosine models, or using multiple breathing periods and averaging them to create one model period. In actuality, respiratory motion is more complex, and studies show breathing changes during treatment [2].

This thesis presents a method to create a more realistic and versatile spatio-temporal model of the moving anatomy for use in 4D cone beam CT reconstruction. It is hypothesized that a set of CT scans has ample information to characterize the tumor motion in a 4D motion model where the motion is continuous for the period of inspection. The method begins with the assumption that an initial 3D source CT scan is available. A 4D deformation model is applied to the source CT to simulate the organ motion. The reconstruction process for the 4DCT is as follows:

- Acquire a CT scan as the patient breathes freely;

- Determine basis vectors and a breathing trace that correspond to the CT scan;

- Apply the 4D deformation model on the initial CT scan to create subsequent simulated projections that change with the organ motion;

- Compare the initial and simulated projection images and use an iterative algorithm to adjust the deformation model until the initial and simulated projection images have a minimum normalized root mean square error.

The proposed method is tested on two data sets using artificial anatomy and projections, artificial motion, and a real breathing trace. The robustness of the 4D reconstruction model is determined by testing the two data sets under ideal and imperfect conditions.

The completed research project is in the area of image-guided adaptive radiation therapy (IGART). The long term goal of IGART research is to enable safe delivery of aggressive radiation treatment by optimal use of imaging technologies coupled with an adaptive delivery system. This requires accurate delineation of the tumor both before and during treatment. In order to obtain precise information regarding the location and shape of the area that needs to be irradiated, a four-dimensional model of the tumor's motion is sought. This model will be used to predict the tumor's location and shape. Our project evaluates the accuracy and robustness of such a model. The completed work assumes a descriptive, rather than predictive, model, and as such provides a better understanding of the tumor's motion. This will allow future research to refine the 4-D motion model to a true predictive model.

CHAPTER 2

BACKGROUND

In this chapter, we briefly discuss some fundamental topics to understand the evolution of four-dimensional computed tomography. In particular, we address the following subjects: computed tomography, radiation therapy, image-guided radiation therapy, and four-dimensional computed tomography.

COMPUTED TOMOGRAPHY

Computed tomography (CT), also known as digital radiography, is an imaging technique that produces a three-dimensional representation of the anatomy through a number of radiologic images from different viewpoints [10]. Over the past decade, CT theory, techniques, and applications have grown tremendously [11]. Therefore, it has substituted many other radiographic exams as the method of choice [6,12].

The computed tomography process begins by taking numerous radiologic x-ray images. Fan-shaped or cone-shaped x-ray beams pass through the patient's body at several angles, and images are taken 360° around the body, along a single axis of rotation [10,12]. The array of detectors and the x-ray tube, separated by 180°, rotate smoothly around the patient, as seen in Figure 1. The detector and the tube exhibit no linear motion [10]. This allows for cross-sectional imaging of the anatomy as well as the continuous acquisition of

the data. The attenuated x-ray transmissions are gathered by an array of several hundred detectors [10,12]. The x-rays that enter the detector array are collimated. This avoids any unnecessary photon scatter as well as keeps radiation exposure and image noise to a minimum. The data acquired by the detectors is digitized into two-dimensional (2D) picture elements (pixels) which are then converted to volumetric elements (voxels), essentially three-dimensional (3D) picture elements [12].
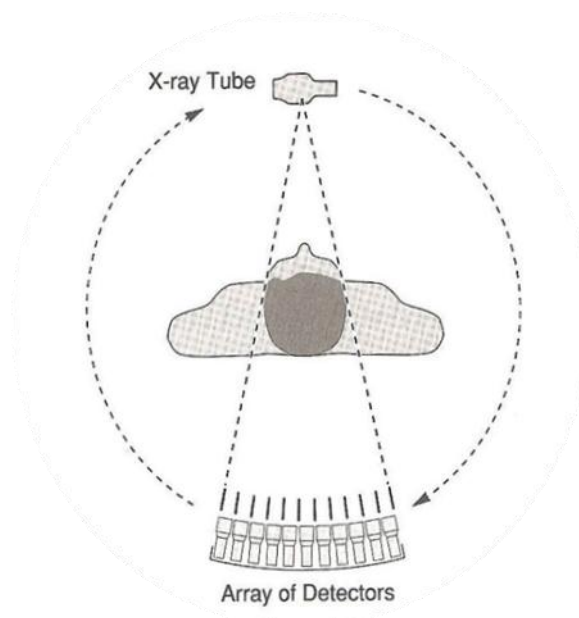
Figure 1: Fan beam CT. The x-ray tube and detector array are 180° apart, with both rotating 360° around the patient. [10]

As stated, CT uses x-rays to create images; consequently, areas of image brightness and darkness depend on the density and presence of atoms with different atomic numbers [10,12]. Tissues within the human body have different physical densities, and the higher the density, the brighter the structure appears on the CT scan [12]. Bone has particularly high density because it is rich in calcium. It will appear white. The lungs, on the other hand, are filled with air and contain very low density, so they appear black. Soft tissues,

such as muscles and organs, and blood appear as various shades of gray. The differences in density allow for the x-ray to be attenuated in distinguishing degrees, thus causing varying degrees of brightness on the CT image. This is commonly referred to as contrast resolution [12]. The gray-scale information digitized into the pixels is reconstructed by using a reconstruction algorithm such as filtered back projection. The gray-scale values within the pixels are defined using Hounsfield Values (otherwise known as CT numbers). The numbers represent the brightness of each pixel (Figure 2).
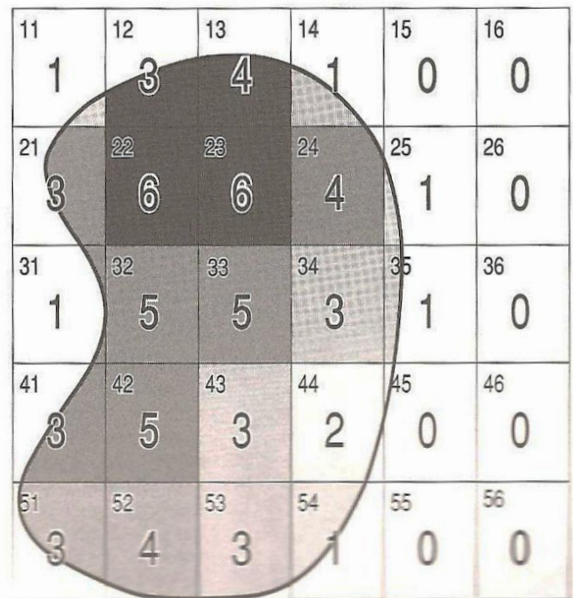
Figure 2: Representation of pixel values, where 0 is the brightest and 7 is the darkest. [10]

CT is advantageous for it allows for the acquisition of volumetric data that outputs high quality images [11]. Benefits include the capability to process and obtain thin cross-sectional images with superior spatial resolution and spatial integrity than other imaging modalities, such as ultrasound, magnetic resonance imaging (MRI), and nuclear medicine [6,12]. Other advantages include depicting bony structure with very good accuracy, as well

as providing relative electron density information. Electron density information becomes useful in calculations for dose distribution [2]. CT also displays precise information of the human anatomy by avoiding the overlay of three-dimensional information onto a single two-dimensional image [12], thus allowing for the use of methods such as tumor localization and treatment in radiation therapy [12].

Disadvantages of CT imaging include the radiation dose received by the patient. A health risk is associated with ionizing radiation. McCollough, et al. states that the radiation dose of one CT scan, 1-14mSv (milli-Sieverts), is equivalent to the annual dose of background radiation (1-10mSv), as with radon and cosmic radiation. Further statistics show that 0.4 percent of all cancers in the United States are caused from CT radiation [6].

RADIATION THERAPY

Radiation therapy is the preferred method of eradicating tumors located in the thorax and abdomen. The radiation is deposited as energy into the patient's body. When human body cells acquire too much energy at one time, they are damaged. They lose their ability to reproduce. Because a tumor is an abnormal growth of cells within the human body, it is necessary to inhibit their reproductive ability. Nevertheless, an unfortunate side effect of radiation is that normal cells in the path of the radiation are also affected. Other uncertainties in radiation therapy planning and treatment include distinguishing the tissues to be radiated and delivering the radiation dose once the tissue is identified [1,2,3]. For this reason, there is a need to locate and differentiate between normal cells and cancer cells during radiation therapy treatment [2,5,7,13,14].

A typical radiation therapy regime consists of five phases: (1) simulation or patient staging, (2) treatment planning, (3) set-up verification, (4) beam delivery, and (5) response assessment or patient follow-up [2,14]. All stages of radiation therapy are heavily dependent on imaging technology.

During the simulation or patient staging phase, the patient is positioned as for treatment delivery with the aid of optical lasers and is immobilized [5,14]. An initial CT scan is conducted to obtain structural information on the patient's anatomy [14]. The information is contained in a three-dimensional data set. The information collected in this data set is used to guide any radiation therapy treatment as well as to position the patient during multiple treatment sessions [5]. During this time, a physical examination of the patient may be conducted as well. The information obtained from the exam may include the location of physical markers on the body. This may be used for positioning the patient or for externally observing respiratory motion during treatment [14]. Once the CT data set is obtained and the physical examination is conducted, the images and information are transferred to the radiation treatment planning phase. Computed tomography is the most used imaging modality in radiation therapy, because of its wide availability, reasonable cost, and ability to extract density information necessary for dose calculation [2,14].

In the radiation therapy treatment planning phase, tumor extension and the organs at risk are determined and assessed [5]. The target volume to treat is also defined. The treatment parameters and the target volume are defined with the information taken from the previous stage. The plan for treatment is calculated with the parameters and is transferred to the next phase, the set-up verification phase. The set-up verification phase

occurs each time the patient is administered radiation. The patient is positioned in the exact manner as in the patient staging and simulation phase. The staging is aided with optic lasers and any physical skin markers. Several imaging modalities are used for positioning the patient; some include ultrasound imaging devices, room mounted kV x-rays, multi-slice CT scanners, and kV or MV cone beam CT scanners [7,13,14]. There is no single device that is appropriate for all situations; therefore, the devices are used on a case-by-case basis.

The radiation delivery is carried out by the treatment device (such as the CyberKNife) according to the parameters of the treatment plan. The tumor is assessed in real time, and treatment is delivered to follow the motion of the tumor. There are temporal changes in the anatomy during treatment, which occur for many reasons. The most prevalent reason for temporal changes in the thorax and abdomen is breathing. Image-guided radiation therapy (IGRT) is used to improve detection of motion, and as a result improve the dose distributions in radiation therapy [1,2,3,4,14].

IGRT is also used for inter-fraction deformation such as rectal and bladder motions [2,14]. It works very well for those cases [14]. In the case of intra-fraction motion, a greater degree of sophistication is required. Cardiac activity and bowel peristalsis are intra-fraction motions that cause changes in tumor motion, but both cases have minor contributions to anatomy motion compared to breathing. The larger temporal changes in anatomy exhibited during radiation therapy is the cause that led to the development of four-dimensional (4D) CT.

The final stage of radiation therapy is the assessment stage. The tumor is assessed after the treatment, and a verdict is made for future radiation therapy. A treatment is determined successful if the tumor size is smaller than the initial size. Imaging modalities similar to those used in the set-up verification stage are used to determine the size of the tumor.

IMAGE-GUIDED RADIATION THERAPY

Image-guided radiation therapy (IGRT) is an in-room image guiding technology which uses instant knowledge of the tumor and changes treatment according to tumor motion and displacement [3]. The purpose of image guided radiation therapy is to reduce the treatment volume with respect to the target volume, and ensure coverage of the target volume without affecting the healthy tissue. Any failure to detect and predict the tumor location restricts the accuracy of the radiation delivered to the cancerous tissue [15].

Computed tomography is the imaging modality that is most widely used for IGRT. In some cases magnetic resonance imaging (MRI) and positron emission tomography (PET) have been used. Computed tomography has many advantages that set it apart from MRI and PET for IGRT. CT gives a very fast scan, depicts spatial information very accurately, supplies electron density information to aid in dose distribution as well as cortical bone information [12,14]. The major drawback of CT is it requires radiation to create images of the anatomy [6,10,11]. MRI does not have this problem; it is a radiation free procedure. It, like CT, is minimally invasive with excellent spatial resolution [10]. Nevertheless, it lacks crucial elements necessary for IGRT. IGRT depends on information of the electron density

of the tissue, and MRI is not able to obtain this information. Unlike MRI, PET is able to provide both anatomical and functional information about the patient, but has low spatial resolution [10]. Other limiting factors with PET are the long data acquisition time and the need for intravenous injection of radiopharmaceuticals [10,14].

Image-guided radiation therapy began with an interest in CT. Current image-guided radiation therapy techniques, such as conformal radiation therapy (CRT) treatment and intensity modulated radiation therapy, use CT imaging. 3DCRT is a method where a 3DCT image of the anatomy is taken, and visualized using computer software. Mathematical algorithms are used to calculate a conformed or focused target area for radiation. Another technique commonly used in image-guided radiation therapy is intensity modulated radiation therapy (IMRT). IMRT, like 3DCRT, uses a 3D image and delivers a high dose of radiation fit tightly around the target volume, with greater dosage to the center and diminished dosage to the outer boundaries of the tumor volume [2,5]. While these technologies provide a means for delivering radiation within the target volume dimensions and sparing healthy tissue, they do so only when the patient is completely immobile [2]. In reality, intra- and inter- organ motions are a significant part of tumor movement [3,14].

FOUR-DIMENSIONAL COMPUTED TOMOGRAPHY

Organ motion in the upper abdomen can move up to 4cm during the breathing cycle. Consequently, 3DCRT and IMRT cannot be fully utilized until temporal motion is accounted for during therapy planning and radiation. Time-dependent imaging is necessary to account for the tumor motion due to breathing [8].

Respiration-induced motion is the most significant source of positional errors in the thorax and abdomen [16]. Internal motion of the body can be classified into inter-fraction and intra-fraction components. Inter-fraction motion occurs through the change in tumor size, either growth or shrinkage, as well as the daily filling and emptying of the bladder and bowel [17]. Motion can also be the result of weight loss or gain between radiation therapy treatment sessions. Intra-fraction motion occurs through organ processes, such as motions related to respiration, the cardiac cycle, or peristalsis of the digestive system [2,17].

Intra-fraction motion, in the thorax and abdomen, is the primary cause for tumor movement. Several studies have determined that the range of motion in the superior-inferior direction of the diaphragm due to normal respiration is approximately 0.5 - 4.0 cm [2,5]. It has also been seen that different areas within the lung exhibit dynamic behavior. The extent of motion in the lungs varies with regions; the lower lobes of the lung exhibit twice the motion of the middle and upper lobes [18-20]. The upper lung has linear motion, while the lower and middle lung regions exhibit less linearity [18]. Lung motion is also prone to hysteresis, with the effects varying though out the lungs [20]. Hysteresis is prevalent in the lower-middle regions of the lungs, and the upper-middle regions show less hysteresis. Motion distorts the target volume to move in and out of the dose targeting window. Subsequently, the area to dose the tumor is increased to compensate for the organ motion. As a result, large amounts of normal tissue are radiated.

The goal of four-dimensional radiation therapy is to deliver high doses of radiation to the tumor, while minimizing the dose to the surrounding healthy tissue [21]. If respiratory motion is not considered when acquiring CT scans, there can be distortion and

deformation of the target volume [17]. There will be large deviations from the planned dose distribution and the actual delivered dose distribution [21]. Including temporal changes in the anatomy during treatment can help reduce dose margins [2,14,15]. A decreased dose margin may lead to reduced radiation toxicity, reduced risk of radiating healthy tissue thus eliminating treatment-induced cancers, and possible dose intensification to the tumor [14,15]. A study conducted by Khan, et al. has shown that using 4DCT over free breathing planned radiation therapy reduces the mean lung dose an average of over 22%. In a particular case the mean lung dose decreased by approximately 38% with 4DCT versus planned radiation therapy [22]. Three common treatment approaches for compensating for respiratory motion are controlled breath hold, respiratory gating, and tumor tracking [23].

In order to suppress respiratory motion, a patient holds his breath during the scanning process of the simulation phase and treatment delivery phase [23,24]. The respiratory motion is eliminated when the breath is held. A static CT scan is obtained during the simulation phase [23]. During each treatment delivery, the patient is expected to hold the breath during dose distribution. The patient is cued, usually visually, as to when to hold and release the breath. The previous process described a voluntary breath hold. Other processes are used frequently in controlled breath hold procedures. One such procedure is active breathing control (ABC), where the respiration is forced to shallow breathing [23]. Treatment is administered during a small window of time. Although this procedure eliminates respiratory motion, it does so with the assumption the patient has the capacity to hold his breath during the scanning process. Many patients have difficulty

13

holding breath, especially those with lung cancer [17,24]. For this reason, there is need for technologies that allow the patient to breathe freely.

Respiratory gating is a technique that allows the patient to breathe freely. The patient's natural breathing pattern is observed, and treatment is delivered periodically when breathing reaches a particular phase [2,14,25]. Usually, the dose is delivered at end-inhale or end-exhale [2]. The patient's respiration is observed and the thoracic wall displacement generally triggers the activation of the radiation dose [26]. Like the controlled breath hold procedure, the initial CT scan taken during simulation must represent the CT sets taken during treatment. A disadvantage of respiratory gating is the active participation of the patient. The patient is required to control breathing to a steady pattern. This is not always possible as there are patients with respiratory complications who are unable to breathe steadily [24]. Another disadvantage is that treatment is longer, since radiation is delivered only over a fraction of the breathing cycle.

Tumor tracking, however, allows for the patient to breathe freely. The delivery field follows the displacement of the target volume during the entire breathing cycle. The field follows the 4DCT set acquired during simulation. Multiple methods have been proposed to increase the accuracy of tumor tracking, but the subject still requires more research.

An accurate method of four-dimensional computed tomography reconstruction is necessary to conduct the previous treatment procedures. 4D imaging focuses on reconstructing a volume that accounts for respiratory motion with minimized motion artifacts [18]. The core cause of motion artifacts is the "transaxial image slicing combined with the asynchronous path of tumor motion" [27].

14

Current practices of 4DCT attempt to include temporal aspects and have been reasonably successful, yet areas that need improvement exist. The standard practice requires the acquisition of large amounts of CT data to reconstruct a complete temporal sequence. A typical three-dimensional CT data set generally contains approximately 100 axial slices, where each slice contains 512x512 pixels. With 16 bits per pixel, a single data set takes over 50 megabytes of storage [2]. Therefore, large data sets increase processing time. Also, as stated previously, larger amounts of data require a greater all around radiation increase to the patient. It is imperative that the amount of data is decreased so patient radiation dose and processing time are decreased.

Some research conducted on reconstructing CT images from incomplete or undersampled data sets involves digital tomosynthesis and prior image constrained compressed sensing (PICCS) [28,29]. Digital tomosynthesis is a method that a reconstructs three-dimensional CT model from two-dimensional radiographic projects using only limited gantry rotation (40° of rotation). The method uses filtered back projection reconstruction methods and does not account for any temporal components. PICCS reconstructs a sparsified image and uses an inverse sparsifing algorithm to construct the target image. This method is able to reconstruct a 3D data set using undersampled projections; however, it does not account for any temporal information.

Another issue with conventional CT practices is how temporal motion is represented. In a typical 4DCT scan, the patient is immobilized and positioned with the help of optical lasers, as with a standard 3DCT scan. The patient's respiratory signal is modeled through one of many methods. Cosine models and piecewise linear models are

methods considered [18]. In some cases fast scanning has been considered. Fast scanning

shortens the rotation time of the scanner to eliminate motion artifacts; this has been

particularly effective in respiratory gating [24].   The more common method used in

modeling respiration for 4DCT reconstruction is using a priori deformation model with a

respiratory trace [16,24,30]. The tidal volume may be measured using a spirometer and

the data collected by the CT machine [14]. Another method uses a physical marker such as

a reflecting block attached to the patient's abdomen, inferior to the xiphoid process. A

camera on the CT machine uses the position of the reflecting block to capture the breathing

pattern of the patient.   The breathing pattern, generally referred to as the respiratory or

breathing trace, is recorded for the entire scan process.   Currently, for the breathing

pattern to be relevant for 4DCT reconstruction, it has to be regular and consistent;

however, research is being conducted for detection and use of irregular breathing patterns

[31,32]. The patient helps in reducing irregularities by breathing calmly and consistently.

They are sometimes prompted by audio cues such as a "breathe in, breathe out" recording.

In some difficult cases, a modified ventilator may even be used to control the airflow [33].

In the conventional method, once the breathing pattern has been established, time

dependent CT projection data is acquired in the helical or cine mode [5,30,34,35]. After an

initial scan is taken, the CT software computes a phase value for every point on the

breathing trace. The end-respiration peaks are detected by the software, and a linear

interpolation method is used to assign percentages, based on the end-respiration peak, to

the remaining points on the trace [14]. The data from the CT scan is partitioned into time

bins corresponding to a user specific time interval. Generally, a time cycle is divided into

10 time bins (Figure 3). The respiratory trace and CT sequences are reconstructed for each

time bin using filtered back-projection into a 4DCT, resulting in ten CTs for the duration of

the breathing period.
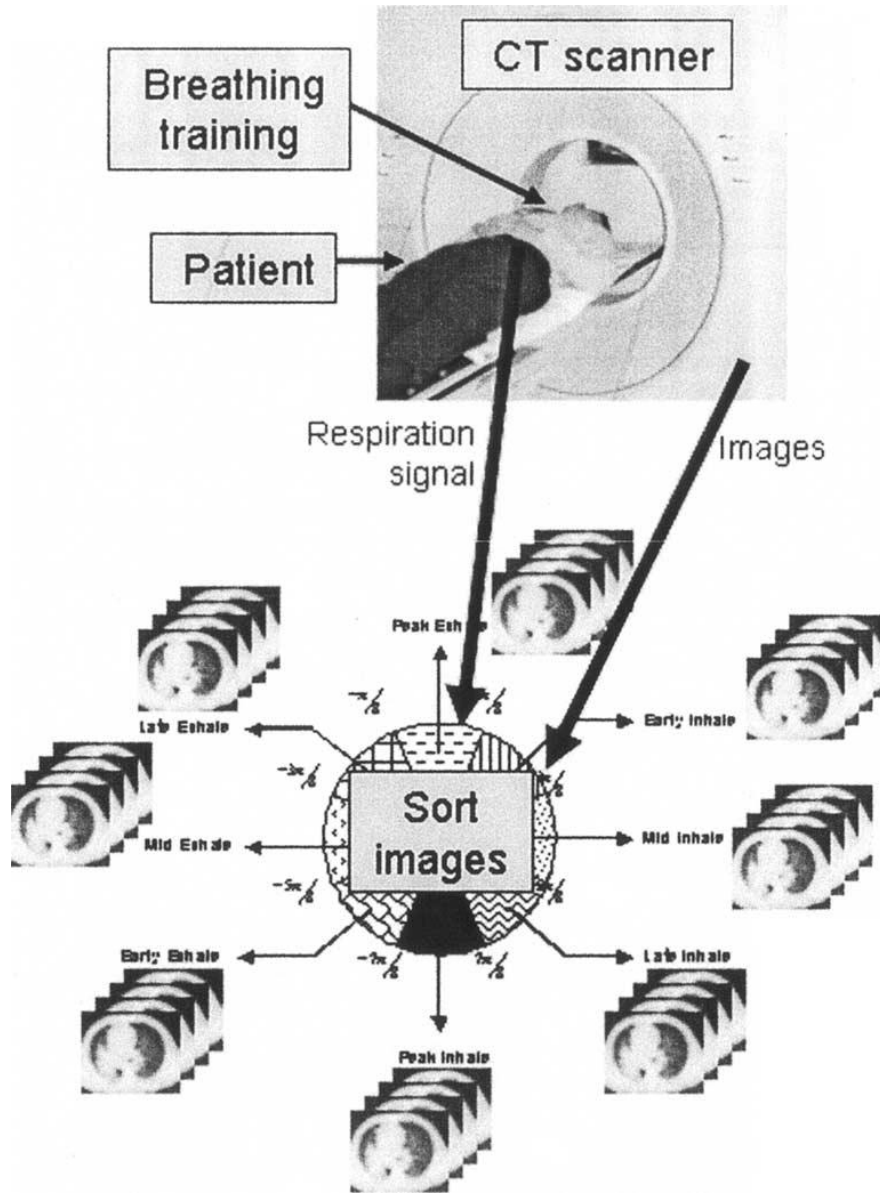
Figure 3: CT images acquired and sorted by phase into time bins
[17]

The treatment planning and delivery phases begin with an assumption that organ motion during the treatment will match the movement observed in the simulation stage. This assumption is not always valid, as a patient may become accustomed to treatment procedures and relax over time [2]. When the patient relaxes, the breathing pattern and rhythm change and breathing becomes shallow. Studies show that over several weeks of radiation therapy, patients have exhibited changes with respiratory motion, even when coached by audio cues [33]. As a result, it is necessary to create a model that allows for changes in the tumor motion.

CHAPTER 3
METHODS AND MATERIALS

The purpose of this work is to create a more realistic and versatile spatio-temporal model of the moving anatomy for use in 4D cone beam CT reconstruction. When modeling anatomy motion, the most challenging factor is achieving a suitable representation of displacement variation in time. A popular approach to model temporal variation is by using a reference CT scan and a breathing trace. The 4D spatio-temporal model in this work is shown by increasing order of complexity and flexibility. This work draws upon the work of Docef and Murphy [9]. We introduce the 4D model in several steps, going from simple to complex.

Step 1: The simplest model assumes the each voxel moves proportionally to the breathing trace. The model is depicted by Equation 3.1. The displacement vector field (DVF) for a specific time location t and spatial location r is represented by $d(t,r)$. The spatial component r is composed of three components in the x, y, and z directions, therefore $r = (x, y, z)$. The breathing trace is represented by b(t), and $u(r)$ is a constant field of amplitudes of which each voxel has three magnitudes along the x, y, and z directions. In this simple model, the every voxel moves on a linear trajectory.

$$d(t,r) = u(r)b(t)$$ (3.1)

Step 2: To increase the versatility of the model, we assume that all the voxels are moving proportionally to the moving trace. We also assume that there is a phase difference (delay) from voxel to voxel; the model is represented by Equation 3.2. Docef and Murphy have modeled the temporal motion using this method. An amplitude and a phase was attributed to each spatial direction (x, y, and z) [9].

$$d(t,r) = a(r)b(t - p(r)) \tag{3.2}$$

Step 3: The next assumption is that the breathing trace is sinusoidal in behavior and model it by $b(t) = \cos(t)$. Therefore, it can be understood that $d(t,r) = a(r)b(t - p(r)) = [a(r)\cos(p(r))]\cos(t) + [a(r)\sin(p(r))]\sin(t)$. The DVF has two components, one in the phase and one in the quadrature. The model is generalized in the following equation:

$$d(t,r) = u_1(r)b(t) + u_2(r)b\left(t - \frac{\pi}{2}\right), \tag{3.3}$$

where $u_1 = a(r)\cos(p(r))$

and $u_2 = a(r)\sin(p(r))$.

Step 4: The assumption for this step is that the signal is no longer sinusoidal, but still is periodic. The breathing signal, $b(t)$, is expressed in terms of its Fourier Series. The following is a case where the Fourier Series has two terms, and it is expressed by assuming $b(t) = \cos(t) + \sin(2t)$. It can be seen that the DVF then has four components as follows:

$$d(t,r) = u_1(r)b(t) + u_2(r)b\left(t - \frac{\pi}{4}\right) + u_3(r)b\left(t - \frac{\pi}{2}\right) + u_4(r)b\left(t - \frac{3\pi}{4}\right) \tag{3.4}$$

where,

$$u_1(r) = a(r)\left[\sin(p(r)) + \cos(2p(r)) - \frac{\sqrt{2}}{2}\sin(2p(r))\right]$$

$$u_2(r) = a(r)\left[\frac{\sqrt{2}}{2}\cos(p(r)) - \frac{\sqrt{2}}{2}\sin(p(r)) - \frac{\sqrt{2}}{2}\cos(2p(r)) + \sin(2p(r))\right]$$

$$u_3(r) = a(r)\left[\sin(p(r)) - \frac{\sqrt{2}}{2}\sin(2p(r))\right]$$

$$u_4(r) = a(r)\frac{\sqrt{2}}{2}\left[\cos(p(r)) - \sin(p(r)) - \cos(2p(r))\right]$$

Each component has a spatial amplitude and a temporal component that is a phase-delayed version of the breathing trace. This representation is not unique, and if we chose a different set of phases of $b(t)$, we get different coefficients. The proof, found in the Appendix, can be extended to any periodic signal. It can be seen that for a breathing signal with N Fourier series terms, we can obtain a DVF with $2N$ components.

Step 5: Finally, the phase delays are considered arbitrary and modeled equation becomes an approximate representation of the DVF (Eq. 3.5). The spatial components $u_i(r)$ can be modeled using spatial models such as B-spline. In this work, we attempt to obtain them from CTs reconstructed via binned filtered back-projection. More specifically, the spatial components are obtained by performing Principal Component Analysis (PCA) or a pseudoinverse matrix method.

$$d(t, r) = \sum_i u_i(r)b(t - \theta_i) \tag{3.5}$$

SOURCE AND TARGET DATA

In this experiment, it is assumed a static initial 4D scan set collected over multiple breathing cycles is available. Additionally, a breathing trace is collected simultaneously with the 3DCT scan. These three components are used to construct a 4DCT reconstruction model. Initially available are a set of deformation vector fields, a source anatomy (the anatomy at the initial point), as well as projections from the source anatomy. A know deformation is applied to the initial anatomy to create a target anatomy. The target anatomy in turn is used to create target CT projections.

Two data sets are used to evaluate the proposed model. Both sets are simulated to be ideal data sets. From Figure 5, it can be seen that data set 2 is designed to have 3 modes that operate separately from each other. Each mode moves with a separate phase and amplitude. This is a simplified case that congruent with realistic data seen in CT projections. Data set 1, however, is designed to be a difficult case for the model. In this case the modes that were described for data set 2 are no longer grouped together. It is designed such that the modes are interlaced in a 1-2-3 pattern. The data seen in data set 1 is a not a realistic representation of tissue motion; nevertheless it is useful for evaluating the robustness of the model in an extreme scenario. In both data sets, the displacement amplitude is maximum in the center of the field of view and decreases towards the edges according to a Gaussian law.

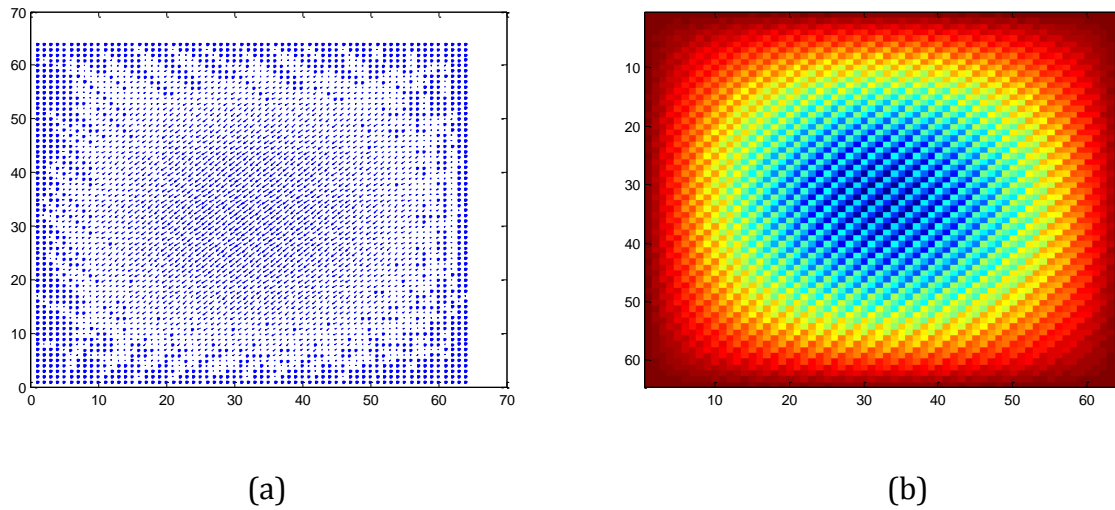(a)   (b)

*Figure 4: Slice from source Deformation Vector Field (DVF) for
Data Set 1. (a) Quiver Plot – shows direction of deformation. (b)
Intensity map – intensity of distribution.*

The source data consists of three dimensional vector fields for multiple time instances, a breathing trace, and corresponding principal components. The deformation vector field has 64 x 64 x 64 voxels over 128 time instances. A slice through the DVF is shown in Figure 4. It can be seen that the DVF has a Gaussian shape. The DVF was downsampled to 32 x 32 x 32 voxels over 32 time instances to reduce memory requirements.

The source anatomy is modeled as a simple structure. The structure of the anatomy is represented by a spherical volume. The region of interest (ROI) of the spherical volume is 1 (dimensionless), and voxels outside of a radius of 0.95 is equal to zero. The volume covers 64 x 64 x 64 voxels, and like the DVF is downsampled during the experiment to 32 x 32 x 32 voxels to reduce memory and computations. The deformed anatomy is modeled by displacing the volume by 10% of the maximum region of interest. The simulation of the

23

anatomy changing through time is made by applying motion to the source anatomy. Also, the source projections and the deformed projections are both created using the source volume. From the volume 32 target projections are created.
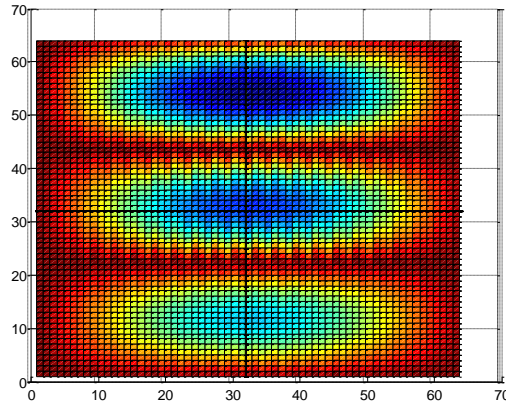
DATA SET 2

*Figure 5: Slice from source Deformation Vector Field (DVF) for
Data Set 2*

Data set 2 differs from data set 1 in the distribution of the DVF. The data DVF has the same size of 64 x 64 x 64 voxels over 128 time instances. The DVF is downsampled to 32 x 32 x 32 voxels over 32 time instances, as with data set 1. Figure 5 shows the DVF to have a different shape. The DVF shows a distribution that consists of three stacked Gaussian distributions.

ITERATIVE MATCHING

The spatio-temporal model considered is based on the most flexible model introduced earlier in the chapter, described by Equation 3.5. The proposed model uses a breathing trace taken over multiple respiratory cycles, and is represented by $b(t)$ (Figure

6). A delay is introduced into the breathing trace and is represented by θ. As stated previously, the phase delay is an arbitrary value, thus allowing the breathing trace to be either periodic or non periodic. The spatial components are modeled by eigenvectors and eigenvalues calculated using principal component analysis (PCA) or basis vectors from the pseudoinverse matrix method.
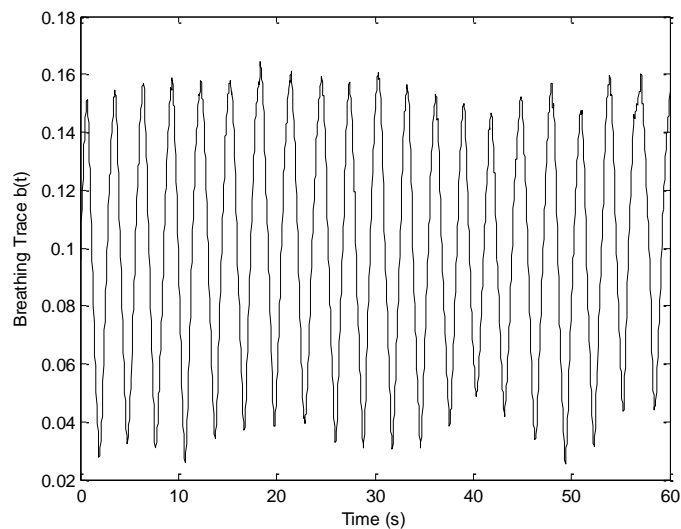

Figure 6: Sample segment of the breathing trace b(t)

PCA is a mathematical procedure that transforms data from one coordinate system or space to another. The data is arranged so that the data with the greatest variance is represented by the first principal component. The first principal component is defined as the largest eigenvalue and its corresponding eigenvector. The data with the second greatest variance, is associated by the second PCA vector. The first two principal components, in general, hold over 90% of the data information. In this experiment we use the first three principal components, because 96% of the data is represented by the first three principal components. The DVF is represented by the following equation.

25

$$d(t,r) = \sum_i a_i b(t - \theta_i) u_i(r) = \sum_{i=1}^{3} a_i b(t - \theta_i) u_i(r) \qquad (3.6)$$

The number of principal components, $u_i(r)$, used in the is model is 3. Three modes were chosen because it was determined to be a suitable number by Vaman, et al [36]. They determined that as each new mode is added, it contributes progressively less to the accuracy of the model. In [36], any contribution from modes greater than three or four can be considered negligible. Although three principal component vectors are chosen for our experiments, 3 is not an ideal number for all sets of data. The number of modes to sufficiently represent a set of data depends entirely on the data itself. The model and associated method for computing model parameters can be applied for more or less basis vectors as necessary. The variable i in equation 3.6 will then range from 1 to the maximum number of modes required.

For equation 3.6, the amplitudes "a" and the phase shifts "θ" are free parameters that are modeled using an iterative procedure. The breathing trace and the principal components are known. The amplitude and phase values are optimized by minimizing the dissimilarity between modeled and measured quantities.. In a first experiment, the deformation model is compared to the source DVF and the difference between the two is used as the similarity measure. The complete set of experiments is described in later sections. The Levenberg-Marquardt iterative optimization method is used to optimize the free parameters. The nonlinear least squares minimization method compares the difference and terminates when the difference of the current iteration is the same as the previous iteration. A tolerance level to stop the iterations is set to 10^{-15}.

An alternative method to model the basis modes is also presented. In the previous case, the basis modes are modeled using Principal Component Analysis vectors. This method assumes, along with a breathing trace, a limited number of DVFs are available; for this experiment we use 8 DVFs. We also assume the delays of the modes are known. Equation 3.6 is modified so that we now solve for the spatial components. The DVFs, $d(t,r)$, are represented by a matrix, where each row is a DVF. The breathing trace is also represented by a matrix, with 3 rows to correspond to the 3 modes. We initially represent Equation 3.6 as a set of matrices, as seen in Equation 3.7.

$$D = BAU \tag{3.7}$$

We expand Equation 3.7 to get Equation 3.8; from this we see for this case that $\boldsymbol{u_1}$, $\boldsymbol{u_2}$, and $\boldsymbol{u_3}$ are the three basis vectors, a_1, a_2, and a_3 are the amplitude parameters, and θ_1, θ_2, and θ_3 are the delay parameters. $\boldsymbol{d_1}$, $\boldsymbol{d_2}$, and $\boldsymbol{d_3}$ are the deformation vector fields and t_1, t_2, and t_3 are the times at which the DVFs are estimated. As stated previously, the experiment uses 8 DVFs, therefore $N = 8$.

$$
\begin{bmatrix} \boldsymbol{d_1} \\ \boldsymbol{d_2} \\ \vdots \\ \boldsymbol{d_N} \end{bmatrix} = \begin{bmatrix} b(t_1 - \theta_1) & b(t_1 - \theta_2) & b(t_1 - \theta_3) \\ b(t_2 - \theta_1) & b(t_2 - \theta_2) & b(t_2 - \theta_3) \\ \vdots & \vdots & \vdots \\ b(t_N - \theta_1) & b(t_N - \theta_2) & b(t_N - \theta_3) \end{bmatrix} \begin{bmatrix} a_1 & 0 & 0 \\ 0 & a_2 & 0 \\ 0 & 0 & a_3 \end{bmatrix} \begin{bmatrix} \boldsymbol{u_1} \\ \boldsymbol{u_2} \\ \boldsymbol{u_3} \end{bmatrix} \tag{3.8}
$$

The following method is used to calculate the matrix U: initially we assume $V = AU$, and then solve for V using the pseudoinverse of B, as shown in Equation 3.9. Then each row of V is normalized to obtain U (Equation 3.10). The spatial components calculated are used as the spatial components $u_i(t)$ in Equation 3.6, and the algorithm is

evaluated using iterative matching. The similarity between the known DVFs and projections versus simulated DVFs and projections is determined using NRMSE.

$$V = B^+ D \tag{3.9}$$

In this equation, B^+ is the pseudoinverse of B.

$$u_i = \frac{a_i u_i}{\|a_i u_i\|} \tag{3.10}$$

EXPERIMENTAL SET-UP

To evaluate the performance of the proposed method, multiple scenarios need to be assessed for both data sets. These scenarios can be grouped into two categories: performance under ideal conditions and performance under imperfect conditions. The model is applied under ideal conditions, initially. This case is when the test DVF can be represented exactly by the 4-D model, with a sufficient amount of CT projections, no noise, and no contrast mismatch. The imperfect scenarios attempt to evaluate the robustness of the model under more realistic conditions, such as the presence of projection noise and contrast mismatch. It is expected that with greater noise and contrast mismatch, the model's performance will be worse than under ideal conditions. A decrease in projection number may also degrade the model's performance.

The performance under ideal conditions compares DVF versus the modeled DVF, volume versus modeled volume, and projections versus modeled projections. The experiment begins with an initial condition of 0 for all 6 free parameters. The number of iterations necessary for convergence is assessed. The effect when the number of

projections is decreased is also considered. Initially 32 projections are considered, then 16, 8, 4, and 2 are also considered.

For the case of imperfect conditions, a DVF that cannot be exactly modeled by the algorithm is considered. Another simulation looks at the effect of white noise in the target data. A random white noise is generated and applied to the DVFs, volume, and projections, specifically 4, 8, 12, 16, and 20 percent of the maximum pixel value. Contrast mismatch is also considered. The pixel values of the target projections are changed using the following nonlinear gamma function (Equation 3.11). 1, 2, 4, 8, 16, and 32 percent of contrast mismatch is explored. Finally the effect of initial conditions is measured. The initial conditions looked at were 0, 25, 50, 75, and 100 percent of the optimal values for the free parameters.

$$p = p - \varepsilon p_{max} \sin\left(\frac{2\pi p}{p_{max}}\right) \tag{3.11}$$

In this equation,

p is the pixel value,

p_{max} is the maximum pixel value, and

ε is the nonlinearity factor.

The prevalent method to measure performance of the model is the mean estimation error. The normalized root mean square error (NRMSE) is the error measure used in this experiment (Equation 3.12). Other methods to evaluate performance are the maximum

estimation error, number of iterations necessary to converge, and the execution time of the optimization.

$$NRMSE = \frac{\sqrt{\Sigma_{r,t}(\hat{d}(r,t)-d(r,t))^2}}{\sqrt{\Sigma_{r,t}(d(r,t)-\bar{d})^2}} \tag{3.12}$$

In this equation,

$d(r, t)$ is the actual DVF,

$\hat{d}(r, t)$ is the estimated DVF, and

$\bar{d}$ is the mean value of the real DVF.

CHAPTER 4
EXPERIMENTAL RESULTS

The reconstruction model is evaluated for accurate and timely convergence. The modeled deformation vector fields and projections are compared to the actual deformation vector fields and projections by means of the normalized root mean square error. The model is determined to be perfectly accurate when the NRMSE converges to zero.

PRINCIPAL COMPONENT ANALYSIS METHOD

PERFORMANCE UNDER IDEAL CONDITIONS

The model is evaluated for ideal conditions, where there is no noise present, no contrast mismatch, and where the DVF can be perfectly matched by the model. The initial condition for each free parameter is zero. The results for data set 1 are shown in Figure 7. It can be seen that the modeled DVF matches perfectly with the actual DVF, when NRMSE equals 0, after six iterations. The DVF error converges to zero percent error in 9 iterations when the volume dissimilarity is used as a target function and in 13 iterations when the projection dissimilarity is used as a target function. DVF matching and projection matching are able to achieve a normalized RMS error of 0% for 32 projections.

31

The same procedure is conducted for data set 2 as for data set 1. The model is evaluated for ideal conditions with zero noise and contrast mismatch with initial conditions of zero for the free parameters. Like with data set 1, it can be seen the DVF, volume, and projections are perfectly modeled by the algorithm. Figure 8 illustrates the number of iterations taken by the model to perfectly match the original data set. The DVF converges to 0% normalized RMS error with 7 iterations, while the volume converges in 8 iterations. The projection takes 38 iterations to converge.
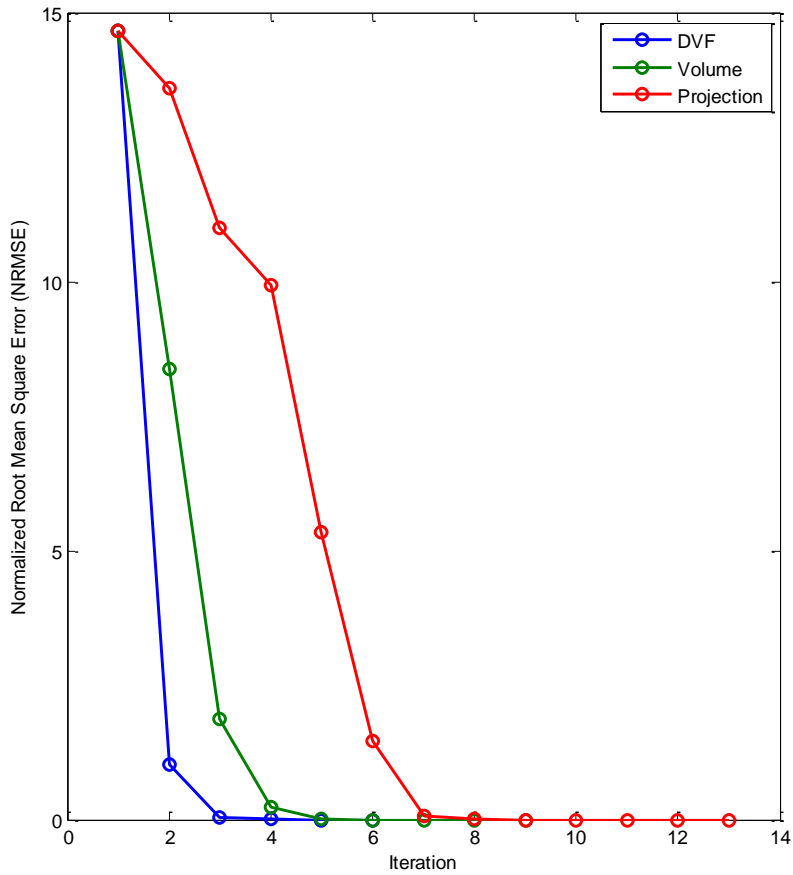

Figure 7: Simulation results for data set 1 under ideal conditions

For both data sets, this is not the case for a reduced number of projections. Table 1 shows that projection matching is not able to produce acceptable results from less than 16 projections. Figure 9 and Figure 10 show for data set 1 and data set 2, respectively, that as the number of projections decrease, the number of iterations to converge increases.
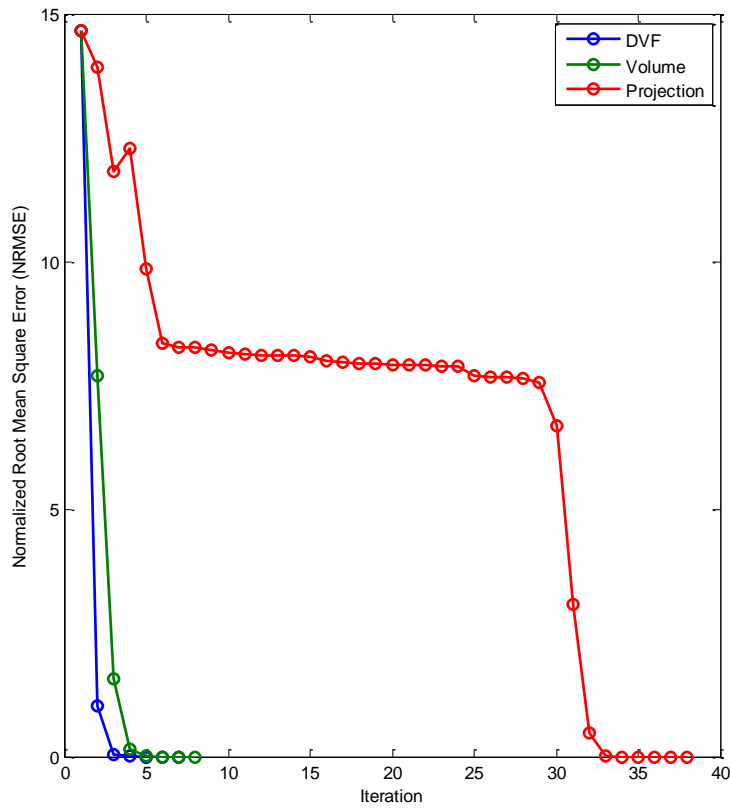

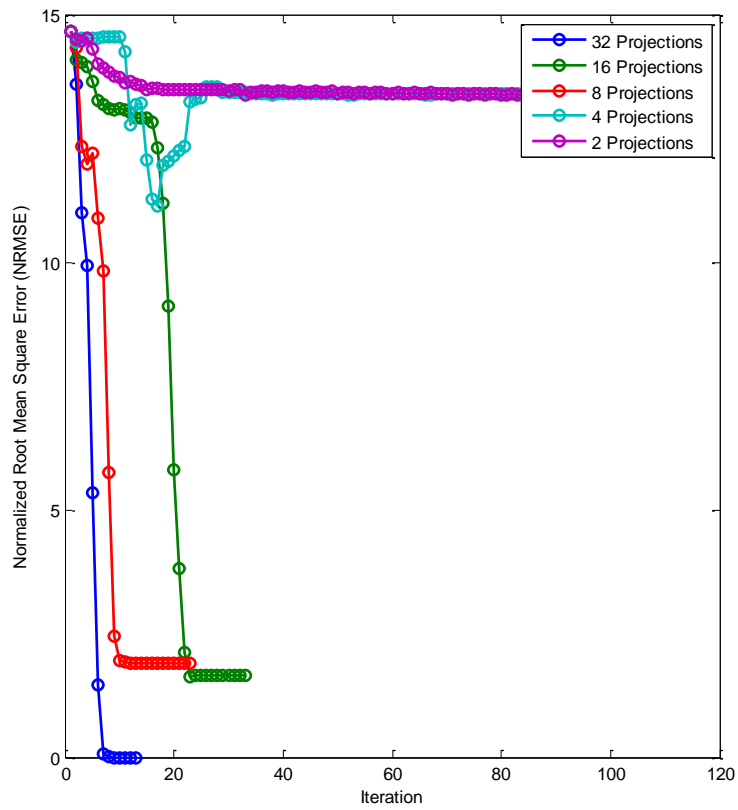*Figure 8: Simulation results for data set 2 under ideal conditions*

Figure 9: Simulation results for effect of reduced number of projections on projection matching for data set 1 under ideal conditions
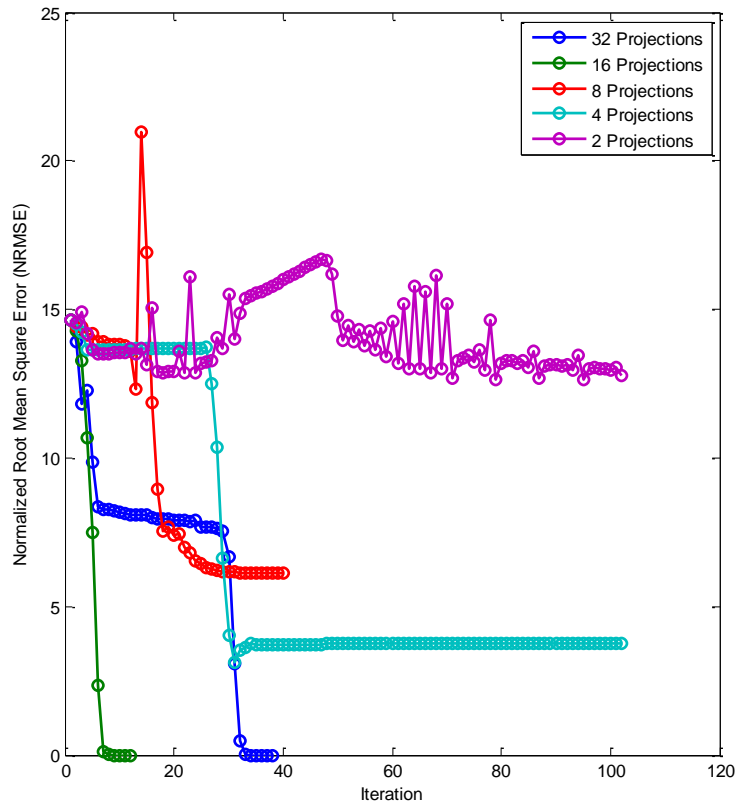
Figure 10: Simulation results for effect of reduced number of projections on projection matching for data set 2 under ideal conditions

Projection Matching	Normalized RMS Error				
No. of Projections	32	16	8	4	2
Data Set 1	0	1.6616	1.9057	13.3888	13.3445
Data Set 2	0	0	6.1089	3.7539	12.7836

Table 1: Results for projection matching for a reduced number of projections for data set 1 and data set 2 using PCA

Experiment 3 considers the effect of initial conditions in optimizing the free parameters of the model. Figure 11 shows the effect of initial conditions for DVF matching and projection matching for data set 1. The results of the simulation for data set 2 are shown in Figure 12. The optimal values for the parameters are initially calculated in order to be used as a benchmark. The initial conditions range from 0 to 100 percent of the optimal value in 25 percent increments. It can be seen the algorithm does not break down as the initial conditions move away from the optimal values.
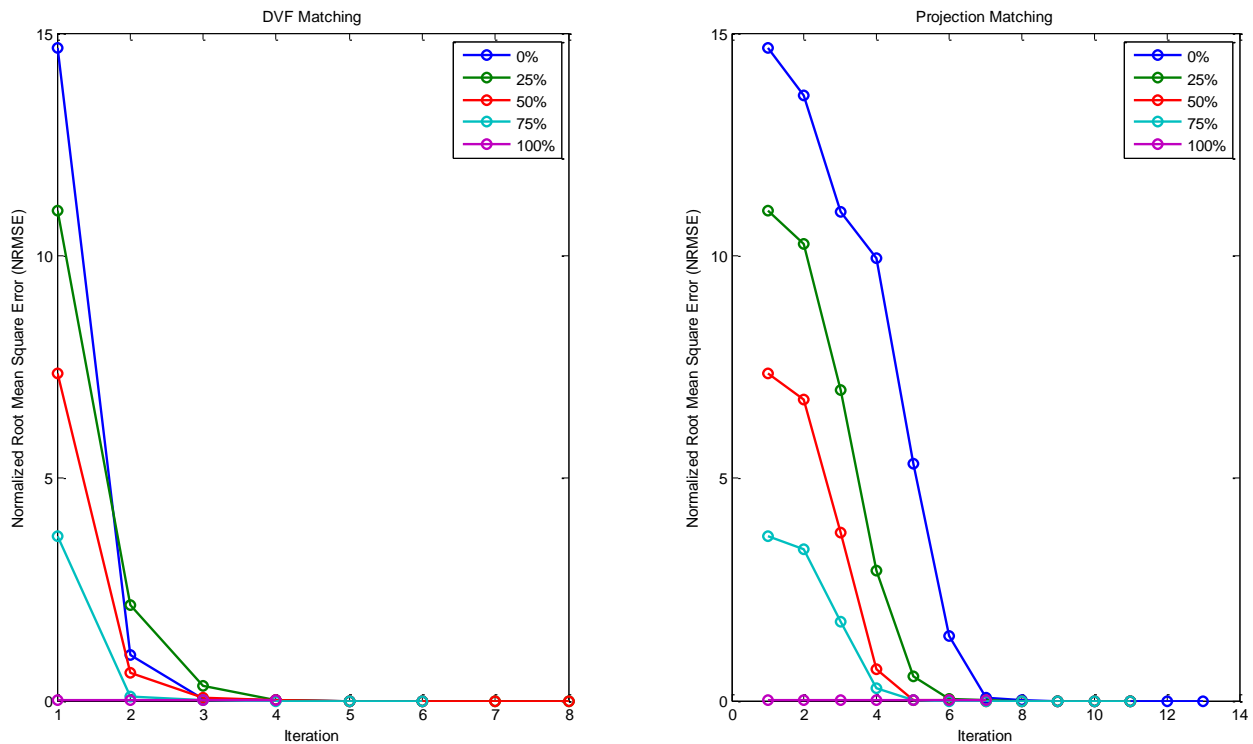

Figure 11: Simulation results for the effect of initial conditions
on DVF matching and projection matching for data set 1 under
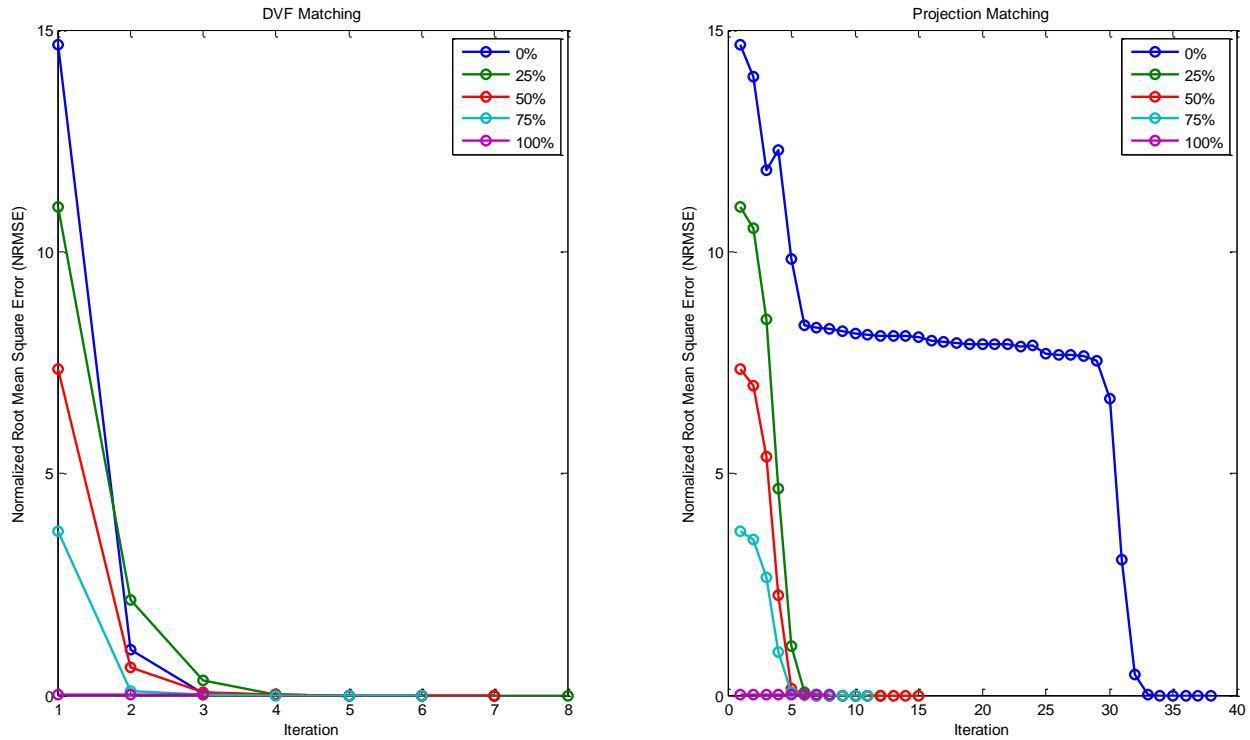*ideal conditions*

Figure 12: Simulation results for the effect of initial conditions on DVF matching and projection matching for data set 2 under ideal conditions

PERFORMANCE UNDER IMPERFECT CONDITIONS

The previous section considered the case where the data is acquired under ideal conditions; here we apply our method to more realistic data. Two cases are explored for non-ideal conditions, the addition of noise and contrast mismatch. The robustness of the algorithm is evaluated using the normalized RMS error. The closer the error is to zero, the more similar it is to the original DVF or projection. Additive noise values are introduced in a range of 0 to 20 percent. Contrast mismatch is introduced according to Equation 3.11, where epsilon values range from 0 to 0.08 (0% - 32%). For data set 1, Figure 13 shows the effect of the addition of noise on projection matching. The results for contrast mismatch

are shown in Figure 15 for projection matching. Figure 14 shows the effect of noise for

projection matching for data set 2. Figure 16 describes the effect of contrast mismatch with
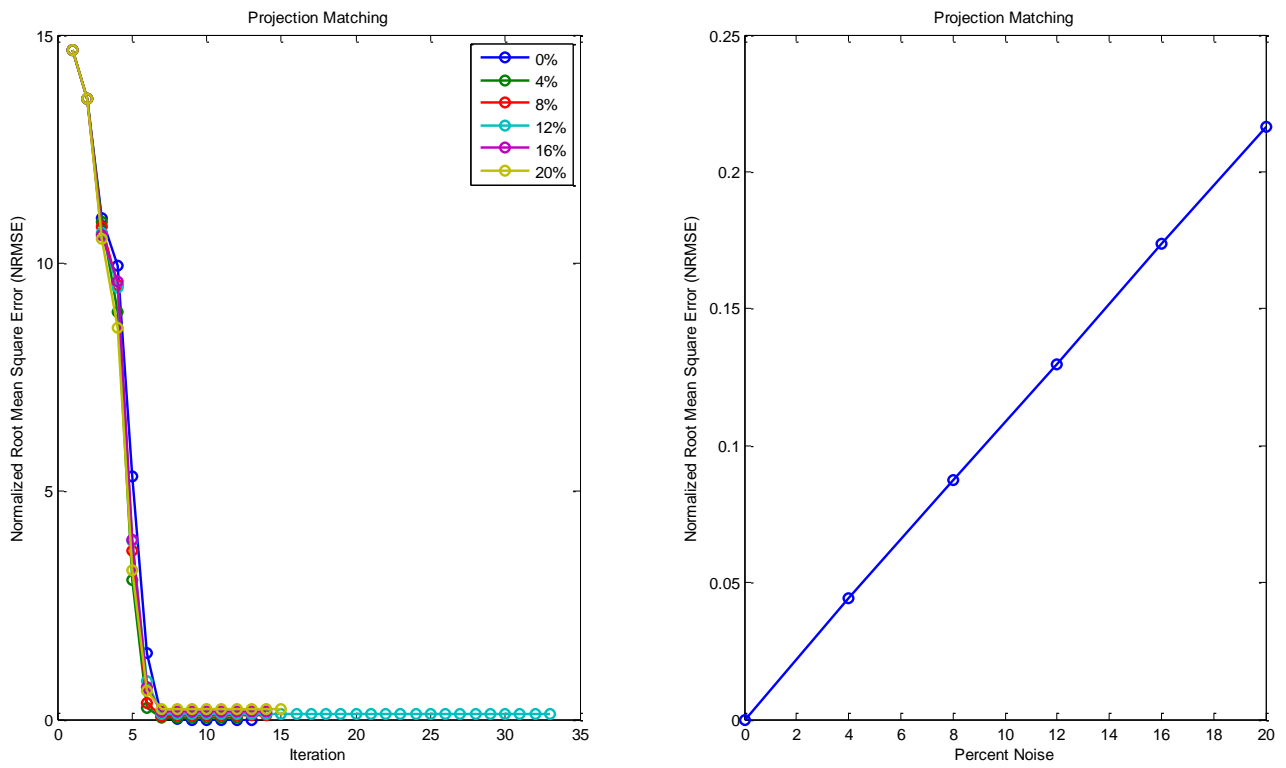
projection matching for data set 2.

*Figure 13:   Simulation results for the effect of noise on
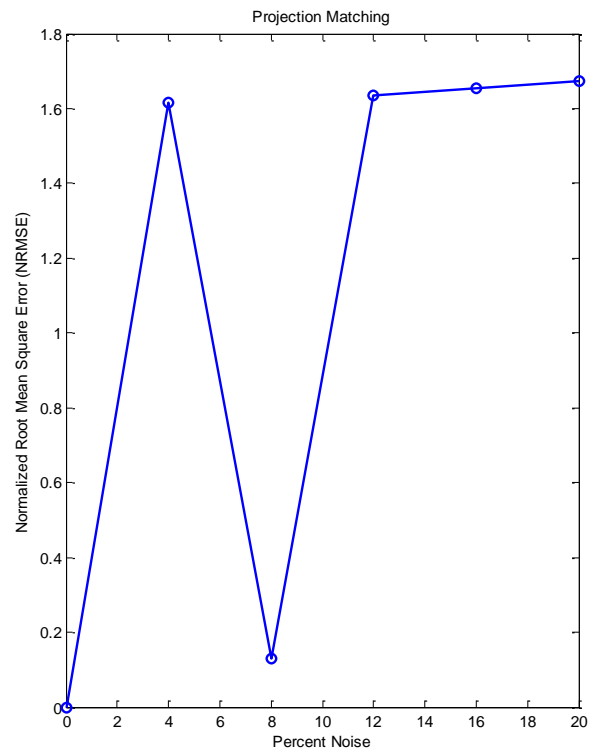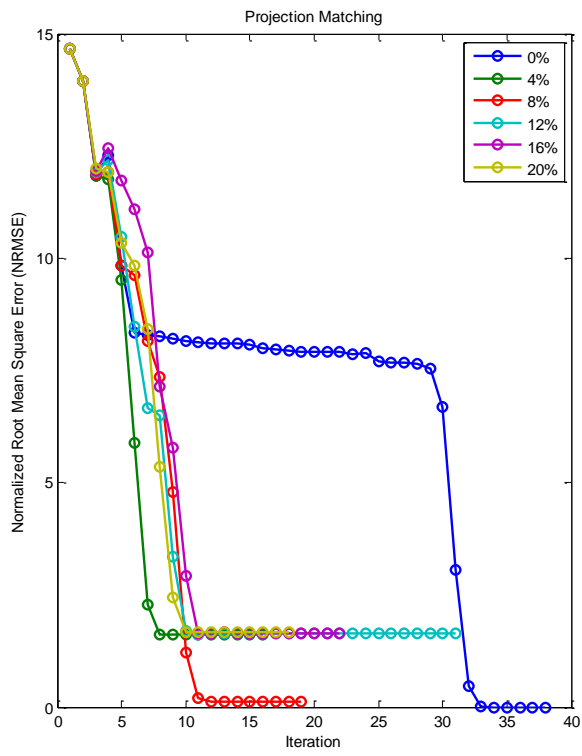projection matching for data set 1 under imperfect conditions*

Figure 14: Simulation results for the effect of noise on projection matching for data set 2 under imperfect conditions
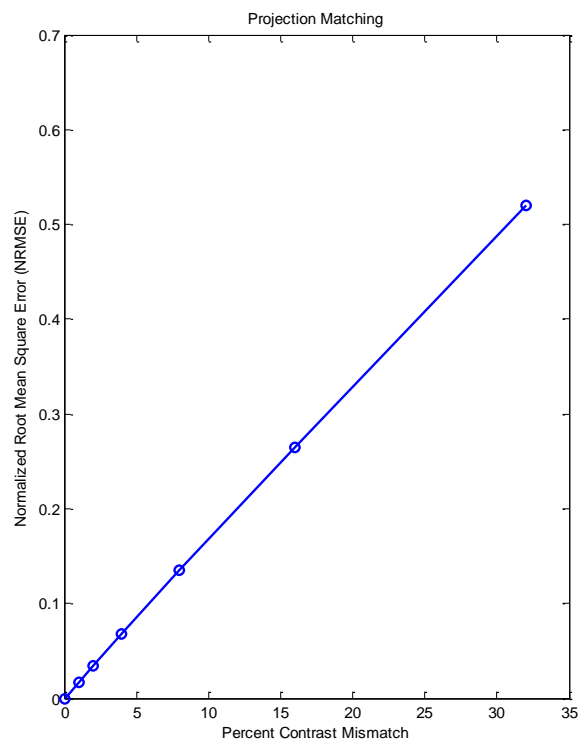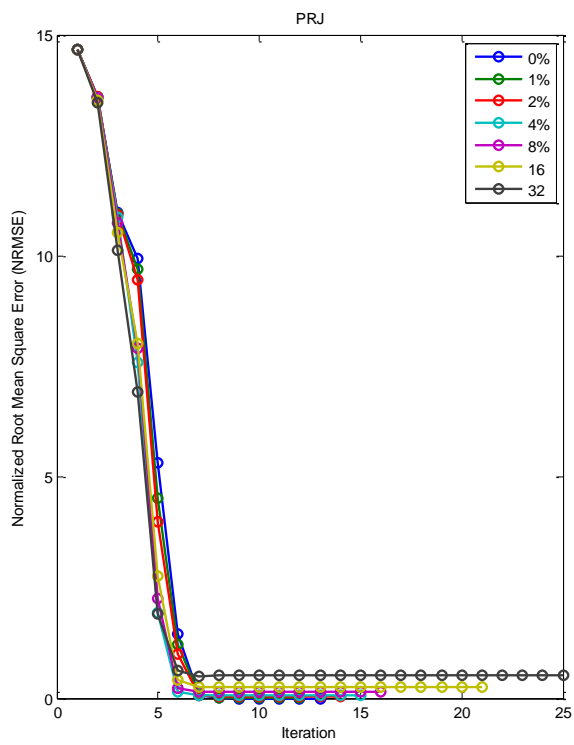
Figure 15:   Simulation results for the effect of contrast mismatch on projection matching for data set 1 under imperfect conditions
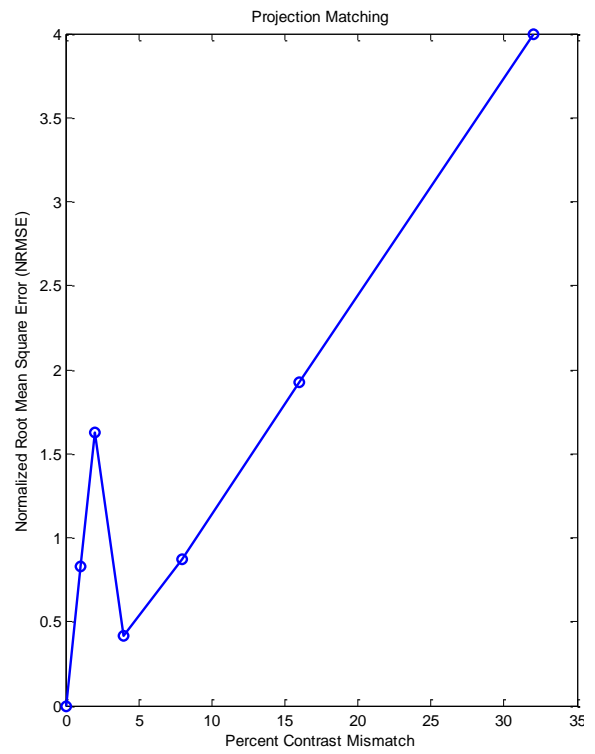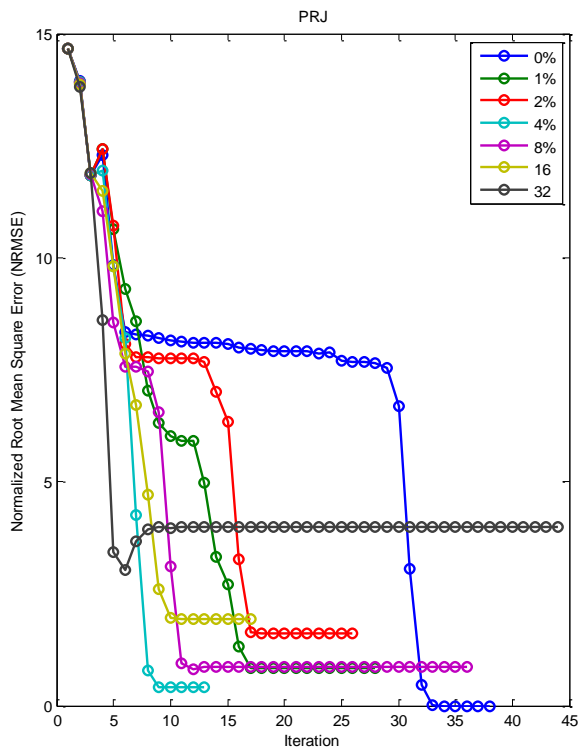
Figure 16: Simulation results for the effect of contrast mismatch on projection matching for data set 2 under imperfect conditions

One more imperfect scenario is considered. The case is explored where the model does not perfectly represent the DVF. For data set 1, it can be seen that the DVF and volume target functions do not converge to 0%, instead to 1.3%, for the normalized RMS error (Figure 17). The projection matching is very inaccurate in representing the actual DVF; it has an error of approximately 225%. This experiment is conducted under the stipulation that there is no noise or contrast mismatch, and the initial conditions equal zero. The effect of initial conditions is explored and depicted in Figure 18. The initial conditions range from 0 to 100 percent in increments of 25 percent of the optimal value. The optimal value for the parameters is calculated by modeling for the DVF of the imperfect case.

Data set 2 also is evaluated for the case where the model does not entirely represent the DVF. The model DVF is compared to the actual DVF and the normalized RMS error is analyzed. The same is done for the volume and projection. It can be seen the DVF converges to an error of 1.3% in 8 iterations, while the volume converges to the same error in 13 iterations. The projection to projection comparison does not converge to the same error value as the DVF and volume. It converges to about 860% error in 102 iterations, as seen in Figure 19. This is conducted with an initial value of zero for all the free parameters. The same case is explored for multiple initial values for the free parameters. The effect of the initial conditions is shown in Figure 20.

Figure 17: Simulation results for data set 1 for a DVF that cannot be perfectly represented by the model
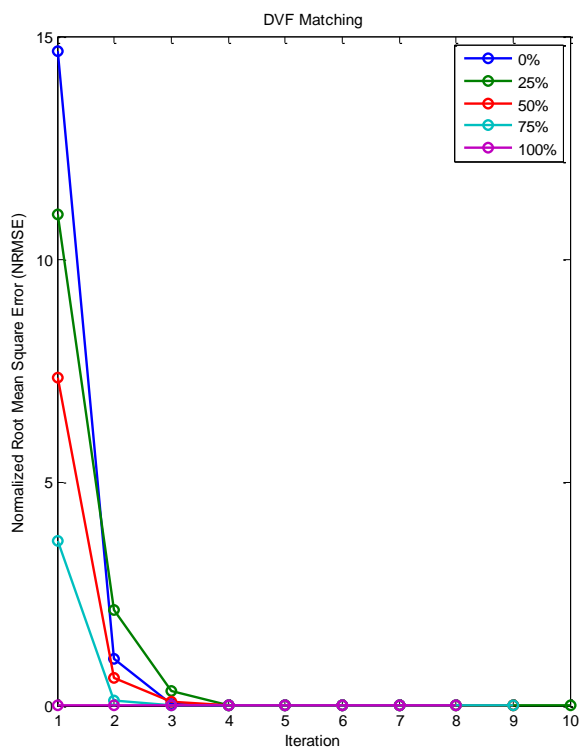
Figure 18: Simulation results for the effect of initial conditions on DVF matching and projection matching for data set 1 for a DVF that cannot be perfectly represented by the model
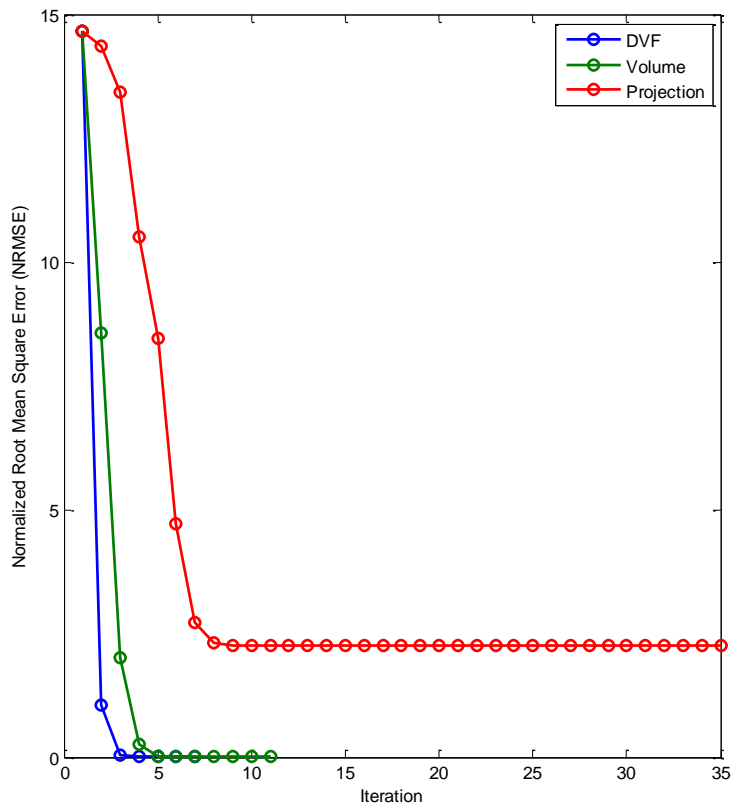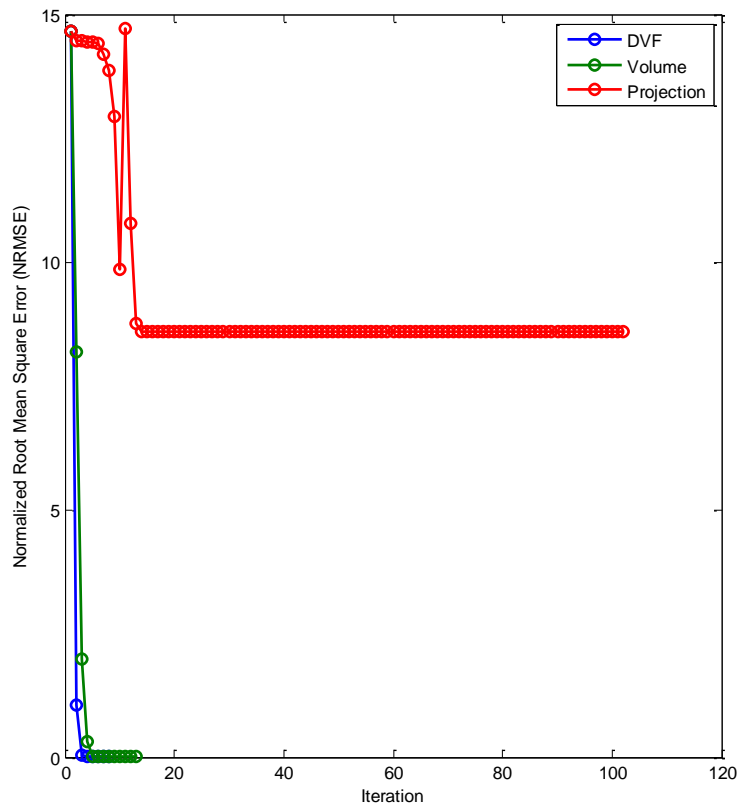
Figure 19: Simulation results for data set 2 for a DVF that cannot be perfectly represented by the model
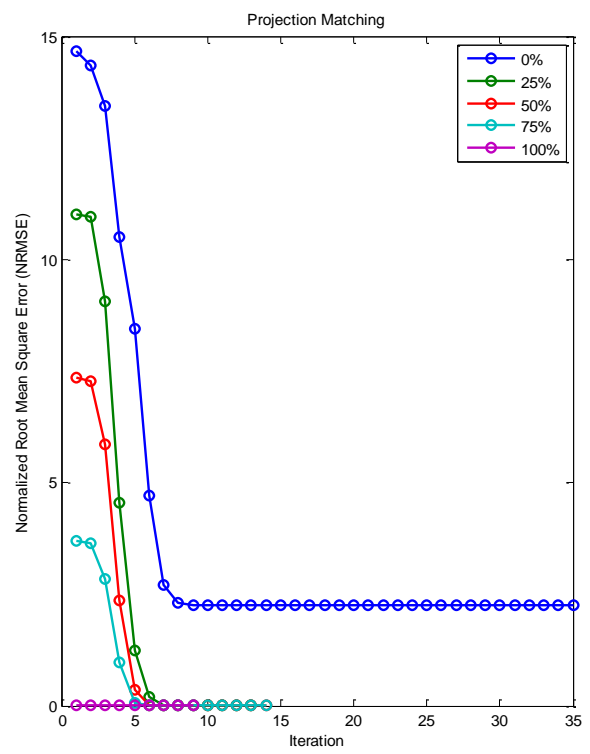
Figure 20: Simulation results for the effect of initial conditions on DVF matching and projection matching for data set 2 for a DVF that cannot be perfectly represented by the model

PSEUDOINVERSE MATRIX METHOD

The same scenarios as the PCA method are considered for the pseudoinverse matrix method. Data set 1 is used to evaluate the performance of this alternative method. Performance under ideal conditions of zero noise and contrast mismatch is considered. Imperfect conditions such as noise, contrast mismatch, and the effect of initial conditions are also considered.

PERFORMANCE UNDER IDEAL CONDITIONS

Figure 21: Simulation results for data set 1 using the pseudoinverse matrix method under ideal conditions

Figure 22: Simulation results for the effect of reduced number of projections on projection matching for data set 1 using the pseudoinverse matrix method under ideal conditions

Projection Matching	Normalized RMS Error				
No. of Projections	32	16	8	4	2
Pseudoinverse matrix method	0	0	1.9056	26.0770	13.0206

Table 2: Results for projection matching for a reduced number of projections for data set 1 using the pseudoinverse matrix method

48

The method is evaluated for zero noise and contrast mismatch with an initial condition of zero for all the free parameters. It can be seen from Figure 21 that the DVF, volume, and projection matching converged to an error of 0%. For DVF matching the optimization process took 7 iterations, and for projection matching it took 10 iterations. The data is downsampled so that 16, 8, 4, and 2 projections are also considered. It can be seen from Table 2 and Figure 22 that for 16 projections and 4 projections the algorithm is able to converge to a normalized RMS of 0. The effects of initial conditions are considered and it is seen that regardless of the initial conditions, the error converged to 0% (Figure 23).

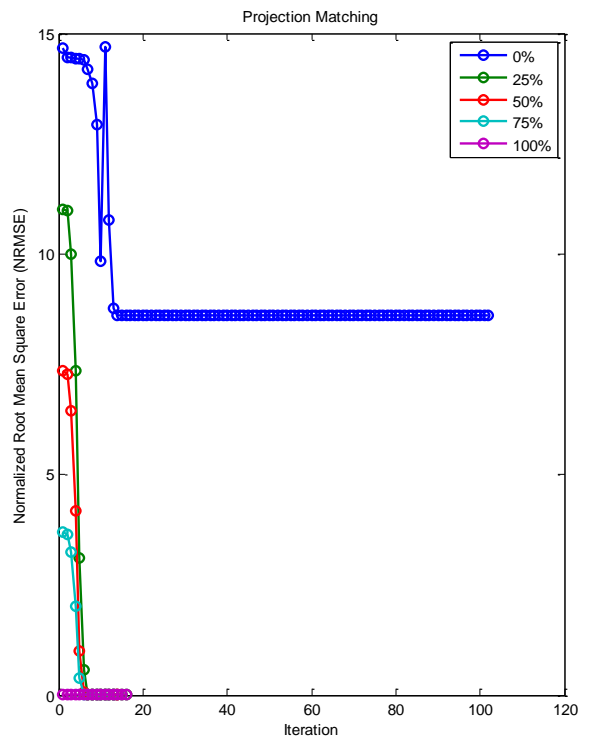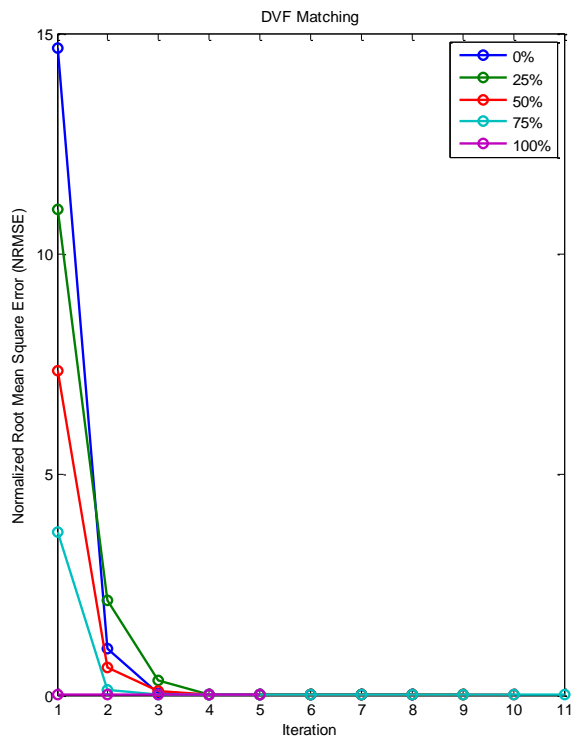*Figure 23: Simulation results for the effect of initial conditions*
on DVF matching and projection matching for data set 1 using
the pseudoinverse matrix method under ideal conditions

PERFORMANCE UNDER IMPERFECT CONDITIONS

The effect of noise and contrast mismatch is also considered. For the pseudoinverse matrix method data set 1 is evaluated for noise values of 0, 4, 8, 12, 16, and 20 percent, and contrast mismatch for 1, 2 4, 8, 16, and 32 percent. The simulation results for noise and contrast mismatch are shown in Figure 24 and Figure 25, respectively.
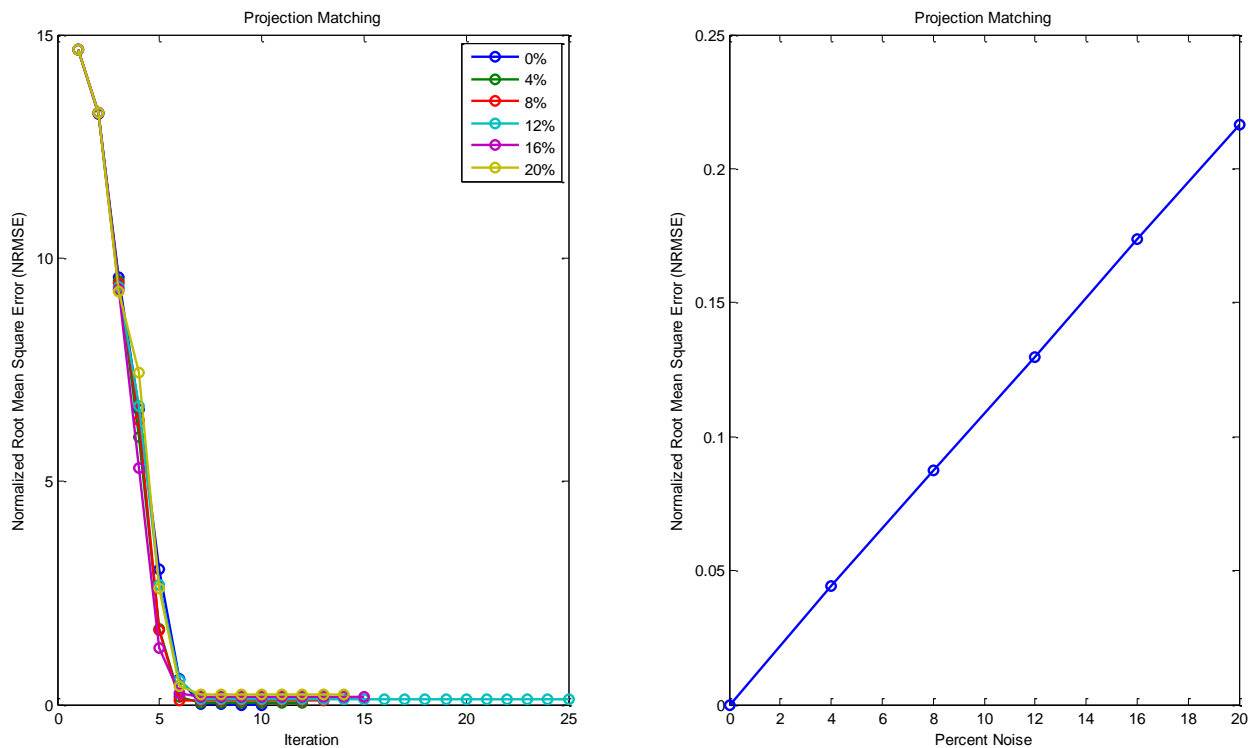
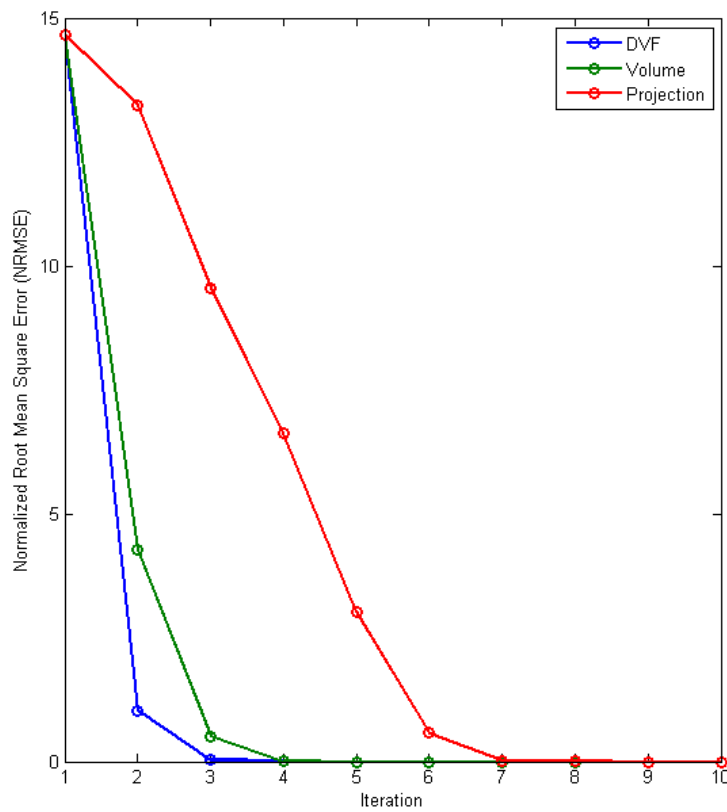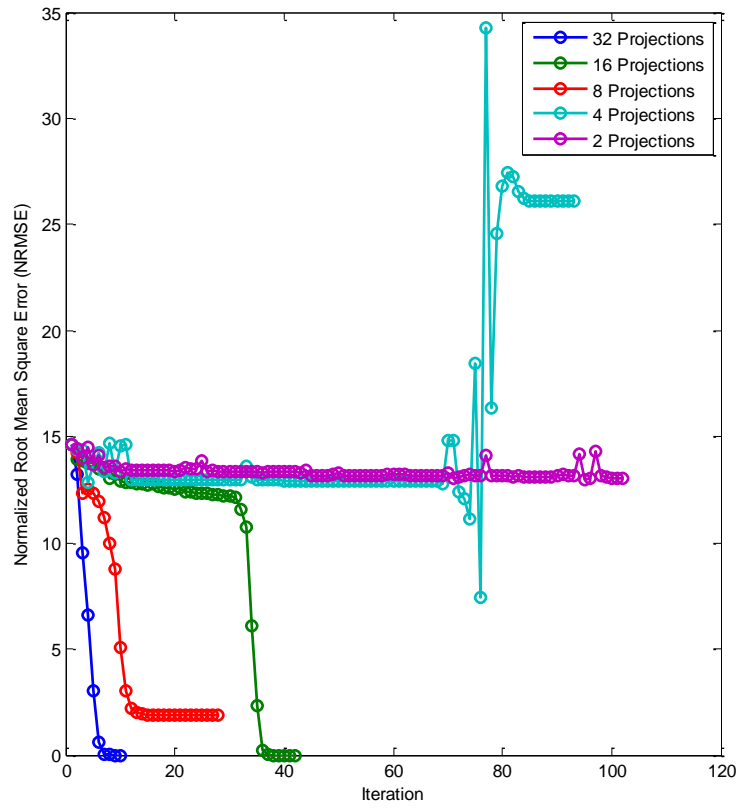*Figure 24: Simulation results for the effect of noise on projection matching for data set 1 using the pseudoinverse matrix method under imperfect conditions*
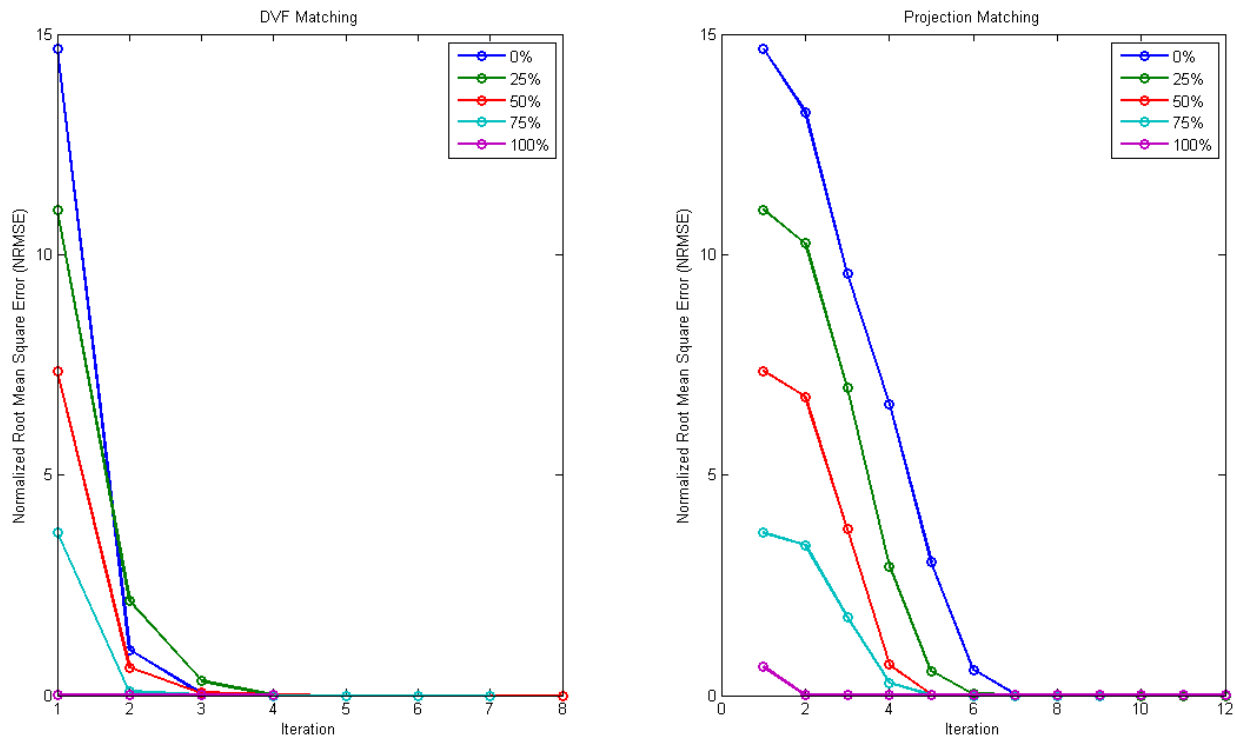
50
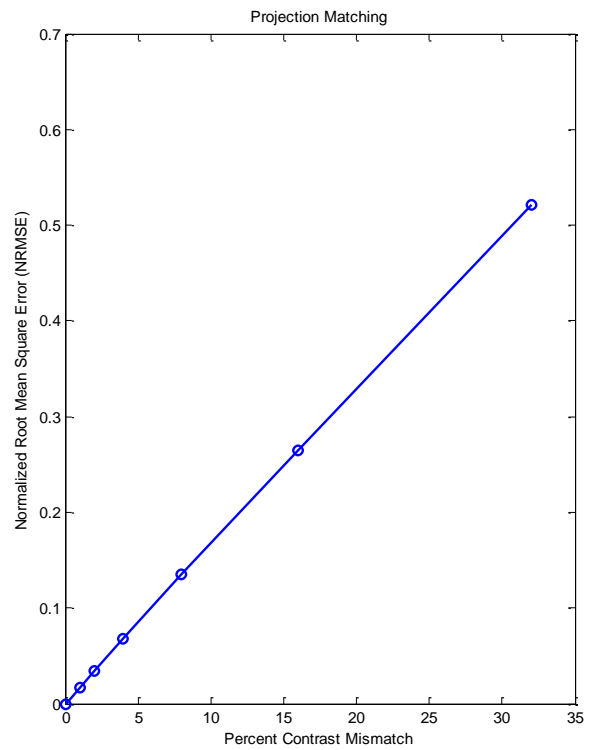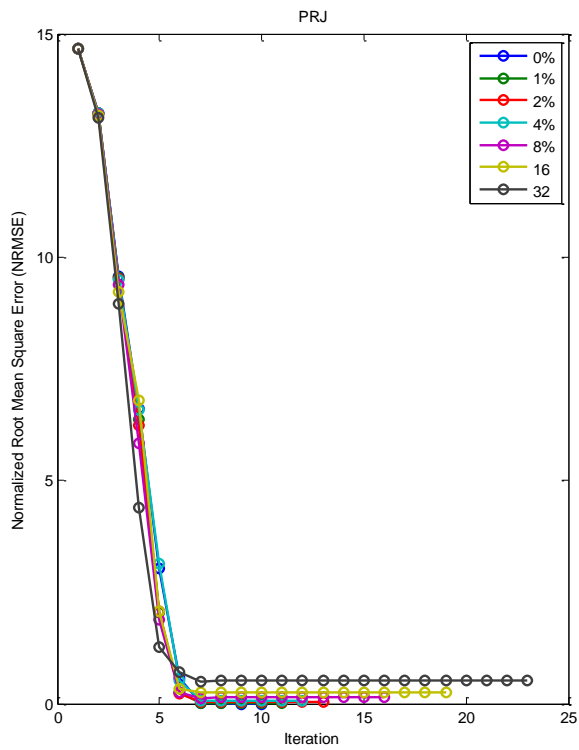
Figure 25: Simulation results for the effect of contrast mismatch on projection matching for data set 1 using the pseudoinverse matrix method under imperfect conditions

CHAPTER 5

DISCUSSION AND CONCLUSIONS

A reconstruction model has been proposed to create a more realistic and versatile spatio-temporal representation for use in 4D CT. The model applies a motion model to a set of CT projections to match the movement in successive sets of CT projections. The model comprises of three components: an initial 4D CT projection set collected over multiple cycles, the breathing trace associated with the set, and the spatial component, a set of basis modes determined using principal component analysis or the pseudoinverse matrix method.

To evaluate the performance of the proposed method, several scenarios have been considered. Two data sets have been tested for two scenarios: performance under ideal conditions and performance under imperfect conditions. Performance under ideal conditions is considered with zero noise and zero contrast mismatch. Imperfect conditions were introduced by adding noise, contrast mismatch, and imperfect modeling. For both cases, the effect of initial conditions in determining the optimum free parameters was considered.

For idealized conditions for the case where the PCA vectors perfectly match the DVFs, the simulated DVF is successfully reconstructed with a normalized root mean square error or 0% for data set 1 and data set 2. For data set 1, the process took 6 iterations of the optimization procedure. Data set 2, a more realistic DVF, converged in 7 iterations. For projection matching, the simulated projections are reconstructed with a normalized RMS error of 0 percent for both data sets. Data set 2 took 38 iterations of the optimization process to converge to 0%, but the more general case, data set 1, of the Gaussian distribution took 13 iterations.

Experiments were conducted to see the effect of downsampling. Thirty two projections were downsampled to 16, 8, 4 and 2 projections. The algorithm broke down for both data sets with 16 projections for projection matching. This is acceptable because typical CT scan projection data sets operate with larger amounts of projections, typically greater than 100 [2]. The algorithm thus proves to be advantageous as it is capable of modeling a data set perfectly with a limited number of projections.

Another such advantage of the algorithm is its independence with respect to the initial conditions estimated for the free parameters. Figure 11 and Figure 12 show the effect of initial conditions on DVF and projection matching for data set 1 and data set 2, respectively. For both data sets, it can be seen that as the initial conditions are closer to the optimal value, the number of iterations are reduced in the optimization procedure than when the values are closer to zero. Nevertheless, the algorithm reconstructs the DVFs and the projections to a normalized RMS error of 0% for both data sets. This is very beneficial because as the initial conditions remain independent of the outcome, it is possible to model

DVF and projections sets where it is not always possible to predict an initial estimate that is similar to the optimal value.

Several scenarios are considered for the performance of the algorithm under imperfect conditions, one of which is the inclusion of noise. It can be seen as the percent of noise increases, the normalized RMS error increases linearly with respect to the noise. This is the case for data set 1 with projection matching, as depicted in Figure 13. It is important to note that the percent of error remains the same with DVF and projection matching, although the number of iterations necessary to converge is greater for projection matching. That is expected because motion information is more obviously presented in a DVF versus a projection. The results for the noise experiments were downsampled from the original projection data both spatially and temporally. It is expected that as the resolution of the projections increases noise will decrease, as the literature shows, projection noise is not correlated in space or time [9,37]. For data set 2, this was not the case. It can be seen that increasing noise did not a linear increase in the error. The model was sensitive to noise with respect to data set 2.

Another parameter that affects data acquisition is contrast mismatch. As with the case for noise, the relationship between normalized RMS error and the percent of contrast mismatch is a linear relationship. An increase in contrast mismatch has shown to produce a less accurate representation of the DVFs and projections. This relationship is relevant for data set 1 using the PCA method. For the case of data set 2, contrast mismatch showed a general linear trend for nonlinearity greater than 4%.

The final case considered is performance of the algorithm for a known case where the DVF cannot be perfectly modeled. In this case it is known that the DVF matching results in an error. The normalized RMS error is found to be 1.3 percent for data set 1 and data set 2. The error is the same for volume matching for both data sets. The error changes for projection matching. Projection matching for data set 1 shows an error of about 225%, and projection matching for data set 2 shows and error of approximately 860%. This experiment is conducted with initial conditions of zero for the free parameters, no noise, and no contrast mismatch.

The error for the projection matching in both data sets is large due to an initial guess of zero for the free parameters. It can be seen from Figure 18 and Figure 20 that initial conditions affect the convergence of the algorithm, unlike with the case where the DVF can be perfectly modeled by the algorithm. For the cases where the initial estimation of the free parameters were from 25 percent of the optimum value to 100 percent, DVF matching and projection matching for both data sets estimated the projections and DVFs to an error of 1.3%. As such, it is determined that initial conditions play a significant role in the ability of the algorithm to converge to an optimal value for the case where the DVF cannot be perfectly modeled.

When the spatial parameters are determined using the pseudoinverse matrix method, it can be seen that the normalized RMS error converged to an error of 0% for DVF matching in 7 iterations, volume matching in 8 iterations, and projection matching in 10 iterations. The projection matching proved to be faster for the pseudoinverse matrix method than the PCA method. As with the PCA method, the projections are downsampled.

The results show for the pseudoinverse matrix method, a reduced number of projections of 16 give a NRMSE of 0%. We can determine that the pseudoinverse matrix method is more robust to a decrease in projections than the PCA method. The final test on ideal conditions, the effect of initial conditions, shows that regardless of the initial conditions, the error converges to 0%. As with the PCA method, it can be seen that the number of iterations increase as the initial conditions move away from the optimal value for the free parameters. When performance under imperfect conditions are considered, it can be seen that the pseudoinverse matrix method and the PCA method produced the same results for noise and contrast mismatch.

The pseudoinverse matrix method is an alternative to using PCA analysis to determine the basis modes. It has the advantage that it can be used to obtain not only the basis modes, but also an estimate of the amplitude parameters of the 4-D DVF model. These amplitude values can then be used as good initial guesses during the projection matching optimization. Its disadvantage is that it requires knowledge of the delays (θ_1, θ_2, and θ_3). These delays could be estimated by using a global signal that can be extracted from the projections without performing 3D reconstruction. Such a signal could be the displacement of the diaphragm, and various averages such as the first and second moments of projections. A method we envision for estimating the delays is based on using a subset of projections acquired at the same gantry angle. Motion information can be extracted from this "video" sequence and used to estimate the delays. The evaluation of such methods is beyond the scope of our work.

It has been seen from the proposed method that it is feasible to estimate an unknown target CT by applying a deformation motion model to the initial CT and by matching the simulated target projections to the original known source projections. The goal of the project is to create a spatio-temporal model for 4D CT reconstruction that can accurately represent the moving anatomy. The goal has been achieved as the model has shown it can accurately reproduce target projections from a limited number of low resolution source projections.

Although the prediction model produces accurate projection data, it breaks down rapidly when constrained by less than 16 projections for the PCA method and by less than 8 projections for the pseudoinverse matrix method. The model is also sensitive to noise and contrast mismatch. There is a linear relationship between noise and error between the source and target projections for data set 1. The sensitivity to noise may decrease with higher resolution projections. It is also seen that data set 2 does not provide a linear relationship with respect to noise and is very sensitive to noise unlike data set 1. It is determined that initial conditions do not influence the accuracy of convergence for the model if the model can perfectly match the DVF. It does, however, affect the convergence speed. As the initial conditions go further away from the optimal value, the convergence speed decreases. The same observation applies in the case where the DVF is not perfectly matched by the model; however, initial conditions do affect the accuracy of convergence. It is determined an initial condition of zero for all the free parameters will not allow the algorithm to converge to the minimum error possible.

This initial investigation shows potential for the algorithm. In the future, further experiments can be designed to evaluate the algorithm (1) with real anatomy, artificial motion, and a real breathing trace, and (2) by using real cone-beam CTs and a real breathing trace.

REFERENCES

[1] Docef A, Murphy MJ, Keall PJ, Siebers JV, Williamson JF. Deformed CT reconstruction from limited projection data. *International Congress Series*. 2005;1281:104-108.

[2] Xing L, Thorndyke B, Schreibmann E, et al. Overview of Image-Guided Radiation Therapy. *Medical Dosimetry*. 2006;31:91-112.

[3] Verellen D, De Ridder M, Storme G. A (short) history of image-guided radiotherapy. *Radiotherapy and Oncology*. 2008;86:4-13.

[4] Brock RS, Docef A, Murphy MJ. Reconstruction of a cone-beam CT via forward iterative projection matching. *Medical Physics*. 2010;37.

[5] Dawson LA, Sharpe MB. Image-guided radiotherapy: rationale, benefits, and limitations. *Lancet Oncol*. 2006;7:848-858.

[6] McCollough CH, Primak AN, Braun N, Kofler J, Yu L, Christner J. Strategies for reducing radiation dose in CT. *Radiol Clin N Am*. 2009;47:27-40.

[7] Dawson LA, Jaffray DA. Advances in image-guided radiation therapy. *J Cin Oncol*. 2007;25:938-946.

[8] Mutaf YD, Antolak JA, Brinkmann DH. The impact of temporal inaccuracies on 4DCT image quality. *Med Phys.* 2007;34:1615-1622.

[9] Docef A, Murphy MJ. Reconstruction of 4D deformed CT for moving anatomy. *International Journal of Computer Assisted Radiology and Surgery*. 2008;3:591-598.

[10] Wolbarst AB. *Physics of Radiology.* Madison, Wisconsin: Medical Physics Publishing; 2000.

[11] Wang G, Yu H, De Man B. An outlook on x-ray CT research and development. *Med Phys*. 2008;35:1051-1064.

[12] Budoff MJ, Shinbane JS. Computed tomography: Overview. In: *Cardiac CT Imaging: Diagnosis of Cardiovascular Disease.* Second ed. London: Springer; 2010:3-20.

[13] Baumann M, Holscher T, Zips D. The future of IGRT - cost benefit analysis. *Acta Oncologica*. 2008;47:1188-1192.

[14] Lecchi M, Fossati P, Elisei F, Orecchia R, Lucignani G. Current concepts on imaging in radiotherapy. *Eur J Nucl Med Mol Imaging*. 2008;35:821-837.

[15] Zhong H, Weiss E, Siebers JV. Assessment of dose reconstruction errors in image-guided radiation therapy. *Phys Med Biol*. 2008;53:719-736.

[16] Mageras GS, Pevsner A, Yorke ED, et al. Measurement of lung tumor motion using respiration-correlated CT. *Int J Radiat Oncol Biol Phys*. 2004;60:933-941.

[17] Keall P. 4-dimensional computed tomography imaging and treatment planning. *Seminars in Radiation Oncology*. 2004;14:81-90.

[18] Boldea V, Sharp GC, Jiang SB, Sarrut D. 4D-CT lung motion estimation with deformable registration: Quantification of motion nonlinearity and hysteresis. *Med Phys*. 2008;35:1008-1018.

[19] Suh Y, Dieterich S, Cho B, Keall PJ. An analysis of thoracic and abdominal tumour motion for stereotactic body radiotherapy patients. *Phys Med Biol*. 2008;53:3623-3640.

[20] Mori S, Endo M, Komatsu S, Yashiro T, Kandatsu S, Baba M. Four-dimensional measurement of lung tumor displacement using 256-multi-slice CT-scanner. *Lung Cancer*. 2007;56:59-67.

[21] Schaly B, Kempe JA, Bauman GS, Battista JJ, Van Dyk J. Tracking the dose distribution in radiation therapy by accounting for variable anatomy. *Phys Med Biol*. 2004;49:791-805.

[22] Khan F, Bell G, Antony J, et al. The use of 4DCT to reduce lung dose: A dosimetric analysis. *Medical Dosimetry*. 2009;34:273-278.

[23] Wong J, Sharpe MB, Jaffray DA, et al. The use of active breathing control (ABC) to reduce margin for breathing motion. *Int J Radiat Oncol Biol Phys*. 1999;44:911-919.

[24] Zeng R, Fessler J, A., Balter JM. Respiratory motion estimation from slowly rotating x-ray projections:Theory and simulation. *Med Phys*. 2005;32:884-991.

[25] Trofimov A, Rietzel E, Lu H, et al. Temporo-spatial IMRT optimization: Concepts, implementation and initial results. *Phys Med Biol*. 2005;50:2779-2798.

[26] Leter EM, Cademartiri F, Levendag P, Flohr T, Stam H, Nowak P. Four-dimensional multislice computed tomography for determination of respiratory lung tumor motion in conformal radiotherapy. *Int J Radiat Oncol Biol Phys*. 2005;62:888-892.

[27] Rietzel E, Pan T, Chen GTY. Four-dimensional computed tomography: Image formation and clinical protocol. *Med Phys 32*. 2005;32:874-889.

[28] Godfrey DJ, Yin F, Oldham M, Yoo S, Willett C. Digital Tomosynthesis with an on-board kilovoltage imaging device. *Int J Radiat Oncol Biol Phys*. 2006;65:8-15.

[29] Chen G, Tang J, Leng S. Prior image constrained compressed sensing (PICCS): A method to accurately reconstruct dynamic CT images from highly undersampled projection data sets. *Med Phys*. 2008;35:660-663.

[30] Low DA, Nystrom M, Kalinin E, et al. A method for the reconstruction of four-dimensional synchronized CT scans acquired during free breathing. *Med Phys*. 2003;30:1264-1283.

[31] Keall PJ, Joshi S, Vedam SS, Siebers JV, Kini V, Mohan R. Four-dimensional radiotherapy planning for DMLC-based respiratory motion tracking. *Med Phys*. 2005;32:942-951.

[32] Taguchi K. Temporal resolution and the evaluation of candidate algorithms for four-dimensional CT. *Med Phys*. 2003;30:640-650.

[33] Yorke E, Rosenzweig KE, Wagman R, Mageras GS. Interfractional anatomic variation in patients treated with respiration-gated radiotherapy. *Journal of Applied Clinical Medical Physics*. 2005;6:19-32.

[34] Keall PJ, Starkschall G, Shukla H, et al. Acquiring 4D thoracic CT scans using a multislice helical method. *Phys Med Biol*. 2004;49:2053-2067.

[35] Ford EC, Mageras GS, Yorke E, Ling CC. Respiration-correlated spiral CT: A method of measuring respiratory-induced anatomic motion for radiation treatment planning. *Med Phys*. 2003;30:88-97.

[36] Vaman C, Staub D, Williamson J, Murphy MJ. A method to map errors in the deformable registration of 4DCT images. *Med Phys*. 2010;37:5765.

[37] Murphy MJ, Wei Z, Fatyga M, et al. How does CT image noise affect 3D deformable image registration for image-guided radiotherapy planning? *Med Phys*. 2008;35:1145-1153.

APPENDIX A
PROOF OF EQUATION 3.4

$$d(t,r) = a(r)b(t - p(r))$$

$$= a(r)\cos(t - p(r)) + a(r)\cos(2t - 2p(r))$$

$$= a(r)\cos(p(r))\cos(t) + a(r)\sin(p(r))\sin(t) + a(r)\cos(2p(r))\cos(2t) + a(r)\sin(2p(r))\sin(2t)$$

$$\begin{bmatrix} b(t) \\ b\left(t - \frac{\pi}{4}\right) \\ b\left(t - \frac{\pi}{2}\right) \\ b\left(t - \frac{3\pi}{4}\right) \end{bmatrix} = \begin{bmatrix} 1 & 0 & 1 & 0 \\ \frac{\sqrt{2}}{2} & \frac{\sqrt{2}}{2} & 0 & 1 \\ 0 & 1 & -1 & 0 \\ \frac{\sqrt{2}}{2} & -\frac{\sqrt{2}}{2} & 0 & -1 \end{bmatrix} \begin{bmatrix} \cos(t) \\ \sin(t) \\ \cos(2t) \\ \sin(2t) \end{bmatrix}$$

$$\begin{bmatrix} \cos(t) \\ \sin(t) \\ \cos(2t) \\ \sin(2t) \end{bmatrix} = \begin{bmatrix} 1 & 0 & 1 & 0 \\ \frac{\sqrt{2}}{2} & \frac{\sqrt{2}}{2} & 0 & 1 \\ 0 & 1 & -1 & 0 \\ \frac{\sqrt{2}}{2} & -\frac{\sqrt{2}}{2} & 0 & -1 \end{bmatrix}^{-1} \begin{bmatrix} b(t) \\ b\left(t - \frac{\pi}{4}\right) \\ b\left(t - \frac{\pi}{2}\right) \\ b\left(t - \frac{3\pi}{4}\right) \end{bmatrix}$$

$$= \begin{bmatrix} 0 & \frac{\sqrt{2}}{2} & 0 & \frac{\sqrt{2}}{2} \\ 1 & -\frac{\sqrt{2}}{2} & 1 & -\frac{\sqrt{2}}{2} \\ 1 & -\frac{\sqrt{2}}{2} & 0 & -\frac{\sqrt{2}}{2} \\ -\frac{\sqrt{2}}{2} & 1 & -\frac{\sqrt{2}}{2} & 0 \end{bmatrix} \begin{bmatrix} b(t) \\ b\left(t - \frac{\pi}{4}\right) \\ b\left(t - \frac{\pi}{2}\right) \\ b\left(t - \frac{3\pi}{4}\right) \end{bmatrix}$$

$$d(t,r) = a(r)[\cos(p(r)) \quad \sin(p(r)) \quad \cos(2p(r)) \quad \sin(2p(r))] \begin{bmatrix} \cos(t) \\ \sin(t) \\ \cos(2t) \\ \sin(2t) \end{bmatrix}$$

$$= a(r)[\cos(p(r)) \quad \sin(p(r)) \quad \cos(2p(r)) \quad \sin(2p(r))] \begin{bmatrix} 0 & \frac{\sqrt{2}}{2} & 0 & \frac{\sqrt{2}}{2} \\ 1 & -\frac{\sqrt{2}}{2} & 1 & -\frac{\sqrt{2}}{2} \\ 1 & -\frac{\sqrt{2}}{2} & 0 & -\frac{\sqrt{2}}{2} \\ -\frac{\sqrt{2}}{2} & 1 & -\frac{\sqrt{2}}{2} & 0 \end{bmatrix} \begin{bmatrix} b(t) \\ b\left(t-\frac{\pi}{4}\right) \\ b\left(t-\frac{\pi}{2}\right) \\ b\left(t-\frac{3\pi}{4}\right) \end{bmatrix}$$

$$= a(r)\left[\sin(p(r)) + \cos(2p(r)) - \frac{\sin(2p(r))\sqrt{2}}{2}\right]b(t)$$

$$+a(r)\left[\frac{\cos(p(r))\sqrt{2}}{2} - \frac{\sin(p(r))\sqrt{2}}{2} - \frac{\cos(2p(r))\sqrt{2}}{2} - \sin(2p(r))\right]b\left(t-\frac{\pi}{4}\right)$$

$$+a(r)\left[\sin(p(r)) - \frac{\sin(2p(r))\sqrt{2}}{2}\right]b\left(t-\frac{\pi}{2}\right)$$

$$+\frac{a(r)\sqrt{2}}{2}[\cos(p(r)) - \sin(p(r)) - \cos(2p(r))]b\left(t-\frac{3\pi}{4}\right)$$

Therefore,

$$d(t,r) = u_1(r)b(t) + u_2(r)b\left(t-\frac{\pi}{4}\right) + u_3(r)b\left(t-\frac{\pi}{2}\right) + u_4(r)b\left(t-\frac{3\pi}{4}\right)$$

where,

$$u_1(r) = a(r)\left[\sin(p(r)) + \cos(2p(r)) - \frac{\sqrt{2}}{2}\sin(2p(r))\right]$$

$$u_2(r) = a(r)\left[\frac{\sqrt{2}}{2}\cos(p(r)) - \frac{\sqrt{2}}{2}\sin(p(r)) - \frac{\sqrt{2}}{2}\cos(2p(r)) + \sin(2p(r))\right]$$

$$u_3(r) = a(r)\left[\sin(p(r)) - \frac{\sqrt{2}}{2}\sin(2p(r))\right]$$

$$u_4(r) = a(r)\frac{\sqrt{2}}{2}\left[\cos(p(r)) - \sin(p(r)) - \cos(2p(r))\right]$$

VITA

Elizabeth Shobha Zachariah was born on August 30, 1986 in Kottayam, Kerala, India and is an American citizen. She was raised in Richmond, Virginia and graduated from Douglas Southall Freeman High School in June 2004. She graduated with a Bachelor of Science in Biomedical Engineering from Virginia Commonwealth University in May 2008. She is currently pursuing her Ph.D. in Electrical Engineering at Virginia Commonwealth University.